Effect of Torque Tube Reflection on Shading and Energy Yield in Bifacial Photovoltaic Systems

Trevor Coathup

A thesis submitted in partial fulfillment of the requirements for the Master of Applied Science degree in Electrical Engineering and Computer Science

School of Electrical Engineering and Computer Science
Faculty of Engineering
Supervisor: Professor Karin Hinzer
University of Ottawa
Ottawa, Canada

February 2023

Acknowledgements

Thank you to my family, Professor Karin Hinzer, Dr. Chris Valdivia, and everyone at Sunlab.

Abstract

Bifacial photovoltaic (PV) modules have greater energy yield than traditional monofacial modules because they convert front and rear incident irradiance to electrical energy. Single-axis tracking systems can further increase energy yield and reduce the levelized cost of energy by rotating the modules throughout the day. However, racking elements in tracking systems introduce both shade and reflections on the rear face, increasing irradiance nonuniformity and fostering further electrical mismatch that reduces module power. The impact of racking, particularly that of the torque tube which spans the middle of the rear collector surface, must be accurately quantified in energy yield predictions to increase stakeholder confidence, and hasten the adoption of tracked bifacial modules.

Isolating the torque-tube-reflected irradiance incident on the modules is crucial for this work. This is achieved by implementing arbitrary two-dimensional (2D) irradiance sampling on a module under test in bifacial_radiance, a ray tracing bifacial PV model, and taking the difference in rear irradiance profiles for simulations with a reflective and an absorptive torque tube at each timestamp. We calculate the TT reflection for the central one-in-portrait (1P) and two-in-portrait (2P) modules on horizontal single-axis trackers over hourly timestamps in a typical meteorological year in Livermore, California, USA.

We introduce the TT reflection 2D irradiance profiles as additional light sources in DUET to quantify the TT reflection's impact on irradiance, electrical mismatch, and energy yield, as well as an incidence angle modifier's impact on TT reflection. We analyze the TT reflection based on sun zenith and diffuse fraction to group consistent illumination conditions across the year.

We identify that TT reflection reduces electrical mismatch by partially offsetting TT shading, and increases annual energy yield by 0.11% and 0.18% in our particular 1P and 2P systems. While the overall impact of TT reflection is greater in the 2P system due to direct beam light incident on the TT, the TT reflection's greatest instantaneous relative contribution to total energy yield is larger for the 1P system, at high diffuse fractions and sun zeniths.

For future work, we recommend validating simulation results with and without TT reflection against experimental data. The simulation method used for isolating the TT reflection may also be repurposed to help inform new TT designs that minimize electrical mismatch. Finally, instead of relying on bifacial_radiance to isolate the TT reflection, we recommend incorporating the TT as a Lambertian reflective surface in 3D view factor models with detailed shading for further TT reflection simulations.

Contents

Publications

The author's research during the pursuit of their degree resulted in the following publications:

Journal Articles:

1. **Trevor J. Coathup**, Mandy R. Lewis, Annie C. J. Russell, Joan E. Haysom, Christopher E. Valdivia, Karin Hinzer, "Impact of Torque Tube Reflection on Bifacial Photovoltaic Single Axis Tracked System Performance," *Manuscript in print with Optics Express*.

2. T. M. Grant, K. L. C. Kaller, **T. J. Coathup**, N. A. Rice, K. Hinzer, and B. H. Lessard, "High Voc solution-processed organic solar cells containing silicon phthalocyanine as a non-fullerene electron acceptor," *Org. Electron.*, vol. 87, p. 105976, (2020); https://doi.org/10.1016/j.orgel.2020.105976

Conference Proceedings:

3. **Trevor J. Coathup**, Mandy R. Lewis, Annie C. J. Russell, Alejandro Conesa, Javier Guerrero-Perez, Christopher E. Valdivia, Karin Hinzer, "Impact of reflective torque tube on rear side irradiance in bifacial photovoltaic modules," *Photonics West*, 2022; https://doi.org/10.1117/12.2615658

4. Mandy R. Lewis, **Trevor J. Coathup**, Annie C. J. Russell, Javier Guerrero-Perez, Christopher E. Valdivia, Karin Hinzer, "Racking Reflection and Shading Effects on Single Axis Tracked Bifacial Photovoltaic Modules," *IEEE 49th Photovoltaic Specialist Conference*, 2022, (under review)

Copyright Permissions

The conference proceeding in Chapter 3 and the manuscript in Chapter 4 are reprinted with permission from all co-authors and the publishers.

Declaration of Originality

Except where otherwise stated, the results presented in this thesis were obtained by the author during the period of their Master's research under the supervision of Dr. Karin Hinzer. They are, to the best of the author's knowledge, original.

List of Figures

Chapter 1: Introduction

Bifacial photovoltaic (PV) modules absorb light through both front and rear faces, leading to increased energy yield. Single-axis tracking systems can further increase energy yield and reduce the levelized cost of energy [1] by rotating the modules throughout the day to maximize the illuminated cross-sectional area, reducing cosine and angle of incidence loses [2]. As a result, the bifacial PV cell market share is expected to grow considerably from 50% in 2021 to 85% in 2032 [3].

Significant strides have been taken to increase accuracy in bifacial PV energy yield predictions and hasten the adoption of bifacial PV including comparisons between software [4], [5], and validation against field data [6]–[13]. However, the bifacial PV market is still maturing, and uncertainty in energy yield prediction can hinder system design and their adoption over alternative investments [14]. In particular, racking elements in bifacial PV systems introduce shading and reflections on the rear face, increasing rear irradiance nonuniformity and electrical mismatch [15]. The effects of racking, particularly from the torque tube (TT) in single-axis trackers as it spans the middle of the rear collector surface and provides the greatest change in irradiance [16], must be accurately quantified in energy yield predictions to further reduce investor risk, increase stakeholder confidence, and hasten the adoption of tracked bifacial PV [14].

Ray tracing bifacial PV performance modeling software [6], [11]–[13], [17]–[20] can model shading and reflections from racking elements at a high computational cost. Two-dimensional (2D) [7]–[9], [21]–[26] and three-dimensional (3D) view factor models [27]–[31] either estimate racking shading with user-defined shading factors determined by comparing PV performance with and without racking [22]–[25], or account for racking shading using simulations of instantaneous ray-object intersection [26]. Hybrid modeling software employ a view factor method for the front irradiance only [5]. One possible enhancement of 3D view factor models with detailed shading accounted for using ray-object intersection is the inclusion of racking reflections, specifically from the TT. However, the isolated impact of racking reflections on PV performance is not well documented.

McIntosh et al. showed that the relative reduction in module power due to nonuniform illumination, including racking shading, is greater for one-in-portrait (1P) than two-in-portrait (2P) single-axis tracker frameless modules, decreasing central module yield by 0.23% and 0.09% respectively [12]. However, the racking reflection's contribution was not isolated. Deline et al. found annual mismatch losses of less than 0.5% for 1P single-axis tracked systems [32].

Guerrero Pérez et al. showed, for a sunny summer day, the rear insolation in a 2P single-axis tracker decreased by 12% with an absorptive TT but only 1.3% with a reflective TT [33].

This work aims to isolate and quantify the impact of TT reflection on irradiance, electrical mismatch, and energy yield for comparable 1P and 2P horizontal single-axis trackers.

This thesis introduces theory and background in Chapter 2 necessary to understand the research described in later chapters. A review of solar cell operating principles is presented, followed by bifacial PV background, and an introduction to the bifacial PV modeling software used in this work.

Chapter 3 presents a conference proceeding for Photonics West 2022, published through the Proceedings of SPIE 11996 in March 2022. This publication calculates the impact of TT reflection on rear insolation, and rear insolation mismatch for 1P and 2P bifacial modules on horizontal single-axis trackers over an hourly typical meteorological year provided by the United States (US) National Solar Radiation Database (NSRDB) [34]. At the time of simulation, bifacial_radiance did not offer features such as including frames on modules, or 2D irradiance sampling of the module(s) under test necessary for determining the irradiance near module edges. These features were implemented by the lead author, T. J. Coathup and are described in the publication.

Chapter 4 of this thesis presents a manuscript in print with Optics Express that builds on the previous publication to include the impact of TT reflection on electrical mismatch and energy yield. We use a hybrid modeling approach with a ray tracing model, bifacial_radiance [11], [17], [18] to extract the TT reflection, and introduce this reflection as an additional irradiance source in DUET [31], a 3D view factor model with detailed shading, to assess the impact of TT reflection in such a model. Using DUET, we can also include and quantify the impact of an incidence angle modifier on the TT reflection's contribution to energy yield. Isolating the TT reflection and accounting for angle of incidence losses was not possible with either simulation method alone, thus bifacial_radiance and DUET were appropriate for this work. Results are analyzed with respect to the sun zenith angle and the fraction of diffuse light to better represent more consistent illumination conditions across the year.

Chapter 5 summarizes the scope of the thesis and provides recommendations for future research on the subject.

Chapter 2: Theory and Background

In order to appreciate how PV systems work and how they are modeled, we begin by introducing the fundamental mechanics and equations that govern PV and solar irradiance.

2.1 Solar Cell Operating Principles

Light is composed of discrete elementary particles known as photons. The energy contained by a photon, E, is given by

$$E = \frac{hc}{\lambda} \tag{1}$$

where λ is the wavelength, h is Planck's constant ($6.626\text{x}10^{-34}$ J·s), and c is the speed of light in vacuum ($2.998\text{x}10^{8}$ m/s) [35].

Solar PV cells convert incident photons to electrical energy through the photovoltaic effect. A photon with energy greater than the semiconductor's bandgap can promote an electron from the valence band to the conduction band, forming an electron-hole pair. A photon with energy less than the bandgap will transmit through the semiconductor. A photon with energy greater than the bandgap will excite the carriers beyond the band edges and lose the additional energy to heat through thermalization back to the band edge. The charge carriers can then be separated, generating current, using the solar PV's built-in electric field. In inorganic semiconductor materials, a sufficient electric field to separate charge carriers can be created by placing an electron-rich, n-type, doped region and an electron-deficient, p-type, doped region beside each other, forming a PN junction. In organic semiconductor materials where charge mobility is lower, two semiconducting materials are often used in conjunction to create a stronger potential gradient and resulting electric field required for charge separation.

Other charge carrier generation processes exist including impact ionization, thermal generation, and impurity-mediated generation. Impact ionization typically is not encountered in a standard solar PV cell as it requires carriers with significant kinetic energy, under high electric field, for example, to promote a valence electron to the conduction band. Thermal generation is caused by high energy lattice vibrations, called phonons. It occurs in all semiconductors to some degree depending on temperature and bandgap, and, to avoid infinite charge accumulation, is necessarily balanced by thermal recombination at equilibrium, resulting in an intrinsic carrier density. Therefore, under illumination, or other non-equilibrium conditions, we are interested in the deviation in carrier populations from the thermal equilibrium values due to additional

carrier generation or recombination. Finally, photons or phonons can interact with localized trap states in the bandgap to generate single free carriers in impurity-mediated generation.

2.1.1 Solar Irradiance

Solar irradiance is the spectrum of light emitted from the sun onto a surface; just outside Earth's atmosphere it resembles a 5800 K blackbody emission. Atmospheric molecules including precipitable water, ozone, oxygen, carbon dioxide, and others preferentially absorb and scatter certain wavelengths, decreasing terrestrial solar irradiance and affecting its overall shape. Moreover, the optical path length of solar irradiance through the atmosphere impacts these light-atmosphere interactions, leading to strong dependencies with sun position based on latitude, time of day, and day of year.

The optical path length of solar irradiance through Earth's atmosphere, L, is often expressed using the air mass (AM) coefficient, a ratio of L to the shortest path length between the atmosphere and the point of terrestrial observation, L_0,

$$\mathrm{AM} = \frac{L}{L_0} \approx \frac{1}{\cos(\theta)} \tag{2}$$

where θ is the zenith angle of incident irradiance. Increasing air mass leads to less energy reaching Earth's surface because the atmosphere attenuates ultraviolet (UV)-visible wavelengths.

Equation 2 approximates AM well for θ up to 75°. For larger zenith angles, we need to account for both refraction and the vertical density profile of atmospheric gases; one common approach is the Kasten & Young fit [36].

$$\mathrm{AM} = \frac{1}{\cos(\theta) + 0.50572(96.07995^\circ - \theta)^{-1.6364}} \tag{3}$$

When specifying air mass, the air mass coefficient is commonly placed immediately after AM. For example, AM1 denotes an air mass of one, with the sun directly overhead. Extraterrestrial irradiance at the interface of space and the Earth's atmosphere is given the unique classification of AM0.

Specific AM1.5 spectra were used by the American Society for Testing and Materials (ASTM) to develop a standard solar spectrum, the ASTM G-173-03, which represents spectral irradiance incident on a plane tilted 37° towards the equator under a single set of specified atmospheric conditions (see Figure 2.1) [37], [38]. This standard is used for testing PV cells and modules

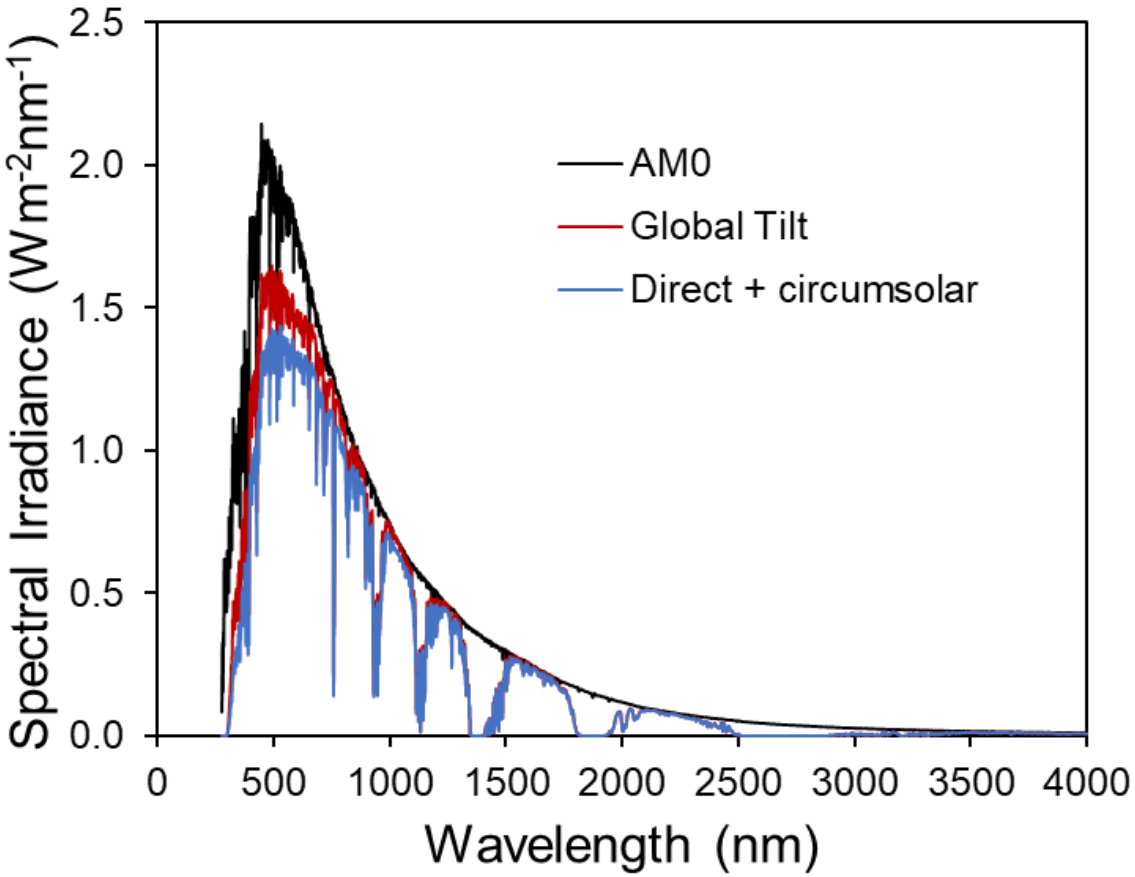

Figure 2.1: Extraterrestrial irradiance at the edge of Earth's atmosphere, AM0, and the reference spectra defined by ASTM G-173-03. The US National Renewable Energy Laboratory provides this standard online [39].

and is intended to represent an average location's average solar irradiance spectrum. Measured spectra deviate from the standard for a plethora of reasons including weather, and sun position.

Given a solar PV's bandgap and a solar spectrum, its maximum theoretical power conversion efficiency, or Shockley-Queisser limit, can be calculated [40]. The Shockley-Queisser limit balances the voltage limit set by the bandgap, transparency losses from photons with energy less than the bandgap, and thermalization losses from photons with energy greater than the bandgap. For crystalline silicon (c-Si) under the standard AM1.5G spectrum, the Shockley-Queisser limit is about 32% [40]. In practice, c-Si solar cells have lower efficiencies due to series and shunt resistances, and carrier recombination.

2.1.2 Recombination

Recombination is necessary to revert the carrier population back to thermal equilibrium after a period of illumination or another non-equilibrium condition. The three types of recombination in bulk semiconductors are radiative recombination, non-radiative (trap-assisted) recombination, and Auger recombination.

Radiative recombination is the process of an electron from the conduction band and a hole from the valence band recombining and emitting a photon with energy equal to the bandgap. Radiative recombination is more probable in direct bandgap materials, like GaAs, than indirect bandgap materials and can set the ultimate limit to efficiency. Non-radiative processes dominate in indirect bandgap materials.

Auger recombination is a non-radiative process where the energy of the photogenerated carrier is dissipated by increasing the kinetic energy of another free carrier. It is the inverse process of impact ionization where a high energy carrier promotes an electron from the valence band to the conduction band, creating an electron-hole pair. Auger recombination is not the dominant recombination pathway in direct bandgap semiconductors because of their short radiative lifetimes. However, Auger recombination dominates in indirect bandgap materials like Si or Ge because Auger processes can conserve momentum.

Finally, impurities in the semiconductor can introduce energy levels within the semiconductor's bandgap, often referred to as trap states, that can capture and then thermally emit free carriers. Trap states near the middle of the bandgap can capture both an electron and a hole, forming a recombination center. Bulk semiconductor trap-assisted recombination, also known as Shockley-Read-Hall (SRH) recombination, can be mitigated by improving the semiconductor material quality.

These three bulk recombination terms can be combined into a net recombination rate for minority electrons in a p-type material under low-level injection,

$$U_n = \Delta n \left(\frac{1}{\tau_{n,\mathrm{r}}} + \frac{1}{\tau_{n,\mathrm{Auger}}} + \frac{1}{\tau_{n,\mathrm{SRH}}} \right) = \frac{\Delta n}{\tau_n} \tag{4}$$

where Δn is the difference in electron concentration from the thermal concentration, n_0, τ_n is the net minority carrier lifetime of electrons in p-type material, and the subscripts r, Auger, and SRH denote radiative, Auger, and SRH recombination processes, respectively.

Recombination can also occur outside the semiconductor bulk at surfaces, interfaces, and, in the case of polycrystalline materials, at grain boundaries. A surface atom in a semiconductor

or an atom at the edge of a crystal lattice has fewer adjacent atoms, leading to dangling bonds. Over the surface of a semiconductor, these dangling bonds and absorbed impurities can form a near continuous distribution of trap states for recombination if the surface is left unpassivated. Passivation helps reduce surface recombination. It is achieved by 1) introducing a layer of fixed charges at the surface to repel minority carriers, or by 2) chemically filling the dangling bonds, usually with hydrogen, or 3) a combination of the two.

2.1.3 Carrier Transport

Before discussing the electrical model of a solar PV cell, it is helpful to understand what governs carrier transport after an electron-hole pair has been generated. Carrier current, **J**, is the sum of drift and diffusion currents for both holes and electrons:

$$\mathbf{J} = \mathbf{J}_n + \mathbf{J}_p = (\mathbf{J}_{n,\text{drift}} + \mathbf{J}_{n,\text{diff}}) + (\mathbf{J}_{p,\text{drift}} + \mathbf{J}_{p,\text{diff}}) \tag{5}$$

where $\mathbf{J}_n$, and $\mathbf{J}_p$ are the electron and hole current densities, respectively, drift refers to the drift component of the current density, and diff refers to the diffusion component of the current density.

Drift current is the motion of charged carriers in an electric field due to the force they experience under the field. Carriers will experience a net velocity called drift velocity, $\boldsymbol{v}_d$, parallel or anti-parallel to the electric field depending on carrier charge. The drift velocity is a function of the electric field, **E**, and mobility $\mu_{\text{e,h}}$ ($\text{cm}^2\text{V}^{-1}\text{s}^{-1}$) of the electron, e, or hole, h:

$$\boldsymbol{v}_\text{d} = \mu_{\text{e,h}}\mathbf{E} = \frac{q\tau_\text{c}}{m^*_{\text{e,h}}}\mathbf{E} \tag{6}$$

where q is the elementary charge of an electron, τ_c is the average time between carrier collisions, and $m^*_{\text{e,h}}$ is the electron or hole effective mass. The drift current density, $\mathbf{J}_\text{drift}$ is now given by the charge and drift velocity of all carriers,

$$\mathbf{J}_\text{drift} = \mathbf{J}_{n,\text{drift}} + \mathbf{J}_{p,\text{drift}} = (nq\mu_n + nq\mu_p)\mathbf{E} = \sigma\mathbf{E} \tag{7}$$

where n and p are the electron and hole carrier densities, respectively, μ_n and μ_p are the electron and hole mobility, respectively, $\mathbf{J}_{n,\text{drift}}$, $\mathbf{J}_{p,\text{drift}}$ are the electron and hole drift current densities, respectively, and σ is the conductivity.

Diffusion current is the motion of free charge carriers from regions of high to low concentration. It follows Fick's first law of diffusion where, under steady state conditions, particle flux is

proportional to the concentration gradient. Thus, the diffusion current density, $\mathbf{J}_{\text{diff}}$ is given by

$$\mathbf{J}_{\text{diff}} = \mathbf{J}_{n,\text{diff}} + \mathbf{J}_{p,\text{diff}} = qD_n \nabla n - qD_p \nabla p \tag{8}$$

where $\mathbf{J}_{n,\text{diff}}$, and $\mathbf{J}_{p,\text{diff}}$ are the electron and hole diffusion current densities, respectively, and D_n and D_p are the electron and hole diffusion coefficients (cm^2/s), respectively. The diffusion coefficient and mobility are related through the Einstein relationships,

$$\frac{D_{n,p}}{\mu_{n,p}} = \frac{kT}{q} \tag{9}$$

Carrier transport, generation, and recombination can be related through the continuity equations which account for the conservation of charge over time for electrons:

$$\frac{\partial n}{\partial t} = \frac{1}{q} \nabla \cdot \mathbf{J}_n + (G_n - U_n) \tag{10}$$

and for holes:

$$\frac{\partial p}{\partial t} = \frac{1}{q} \nabla \cdot \mathbf{J}_p + (G_p - U_p) \tag{11}$$

where G_n and G_p are the generation rates of electrons and holes, respectively, and U_n and U_p are the recombination rates of the electrons and holes, respectively.

Equations 10 and 11 can be simplified by restricting the analysis to one dimension, assuming mobility is spatially uniform, and by applying the equations for drift and diffusion current:

$$\frac{\partial n}{\partial t} = \mu_n n \frac{\partial E}{\partial x} + \mu_n E \frac{\partial n}{\partial x} + D_n \frac{\partial^2 n}{\partial x^2} + G_n - U_n \tag{12}$$

$$\frac{\partial p}{\partial t} = \mu_p p \frac{\partial E}{\partial x} + \mu_p E \frac{\partial p}{\partial x} + D_p \frac{\partial^2 p}{\partial x^2} + G_p - U_p \tag{13}$$

Further simplifications are possible in devices dominated by minority carriers, such as solar cells, where we restrict the analysis to minority carriers. For instance, solar cells are often under constant illumination, i.e., steady state conditions, making the left-hand side of Equations 12 and 13 both zero. We also assume low-level injection, and are interested in the quasi-neutral regions of the diode where $E \approx 0$. Thus, the first and second terms on the right-hand side of Equations 12 and 13 are zero. In addition, we are only interested in the derivatives with respect to excess electron and hole populations because their thermal concentrations, n_0 and p_0, are assumed to be uniform with respect to position. Furthermore, electrons and holes are generated in pairs because only photogeneration is possible, making $G_n = G_p \equiv G_{\text{L}}$. Finally, under low-level injection, the net recombination terms can be replaced with Equation 4 and the analogous equation for minority holes in an n-type material.

Applying the above simplifications yields the minority carrier diffusion equations:

$$0 = D_n \frac{\partial^2 \Delta n_p}{\partial x^2} + G_{\mathrm{L}} - \left(\frac{\Delta n_p}{\tau_n} \right) \tag{14}$$

for minority electrons in a p-type material, where Δn_p is the difference in minority electrons from the thermal concentration, n_0, and:

$$0 = D_p \frac{\partial^2 \Delta p_n}{\partial x^2} + G_{\mathrm{L}} - \left(\frac{\Delta p_n}{\tau_p} \right) \tag{15}$$

for minority holes in an n-type material, where Δp_n is the difference in minority holes from the thermal concentration.

2.1.4 The pn Diode in the Dark

Equations 14, and 15 are solved with a final approximation where it is assumed that the space charge region is fully depleted of mobile carriers up to the edges of the depletion region. They may be coupled with Equation 8 to approximate a single diode in the dark, where G_L is zero.

$$J(V) = J_{0,\mathrm{diff}} \left(e^{qV/kT} - 1 \right) \tag{16}$$

This is the ideal single diode equation, where $J_{0,diff}$ is the saturation current density due to carrier diffusion in the quasi-neutral region, V is the voltage, k is the Boltzmann constant, and T is absolute temperature. It is common for modeling the behaviour of most solar cells. Space charge region generation and recombination can be accounted for using the last term in

$$J(V) = J_0 \left(e^{qV/kT} - 1 \right) + J_{0,\mathrm{SCR}} \left(e^{qV/2kT} - 1 \right) \tag{17}$$

where $J_{0,SCR}$ is the saturation current density due to space charge region recombination. It depends on the depletion region width and carrier lifetimes. The exponential for the space charge region term is notably half the diffusion term's exponential. However, the saturation current from space charge region recombination is larger than that from diffusion and it dictates the current for low voltages. At higher voltages diffusion will dominate. In some devices, the regions are not so easily distinguishable. For such occasions, the saturation current density terms may be amalgamated to a single term, J_0, with help from a fitting factor, m, the ideality factor:

$$J(V) = J_0 \left(e^{qV/mkT} - 1 \right) \tag{18}$$

This is the single diode equation. The ideality factor ranges from $m = 1$, an ideal diode, to $m = 2$, a space-charge-region-limited diode, to fit device performance. Equation 18 is used in the modeling sections of this work to calculate solar cell performance.

2.1.5 Solar Cell Circuit

In an ideal solar cell, the current is given by a photogenerated current source in parallel with a single diode, as shown in Figure 2.2.

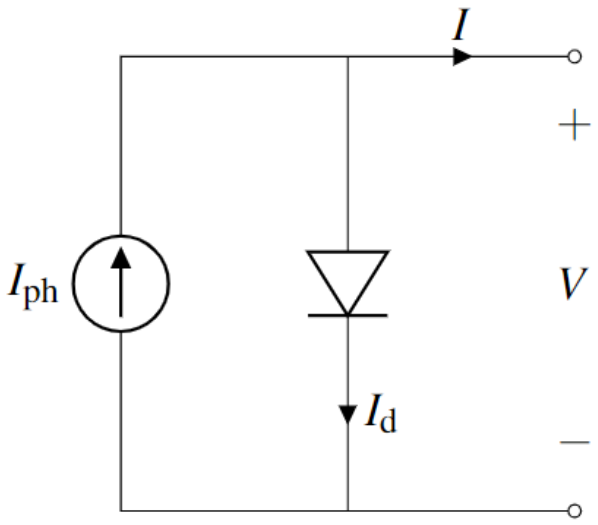

Figure 2.2: Ideal solar cell equivalent circuit.

By superposition, the net current flowing through the cell, I, is given by

$$I(V) = I_0 \left(e^{qV/kT} - 1 \right) - I_{ph} \tag{19}$$

where I_0 is the saturation current and I_{ph} is the photogenerated current. This is the same as the ideal diode in the dark but shifted down by I_{ph}.

Several key parameters for quantifying solar cell performance are derived from Equation 19. They include: the short-circuit current, I_{sc}; the open-circuit voltage, V_{oc}; the maximum power, P_{max}; and the fill factor, FF. These are labeled in Figure 2.3. Following convention, the current is flipped for convenience.

The power is given by the product of current and voltage. The maximum power the solar cell can produce is given by:

$$P_{max} = I_{mpp} V_{mpp} \tag{20}$$

where I_{mpp} is the current at the maximum power point, and V_{mpp} is the voltage at the maximum power point.

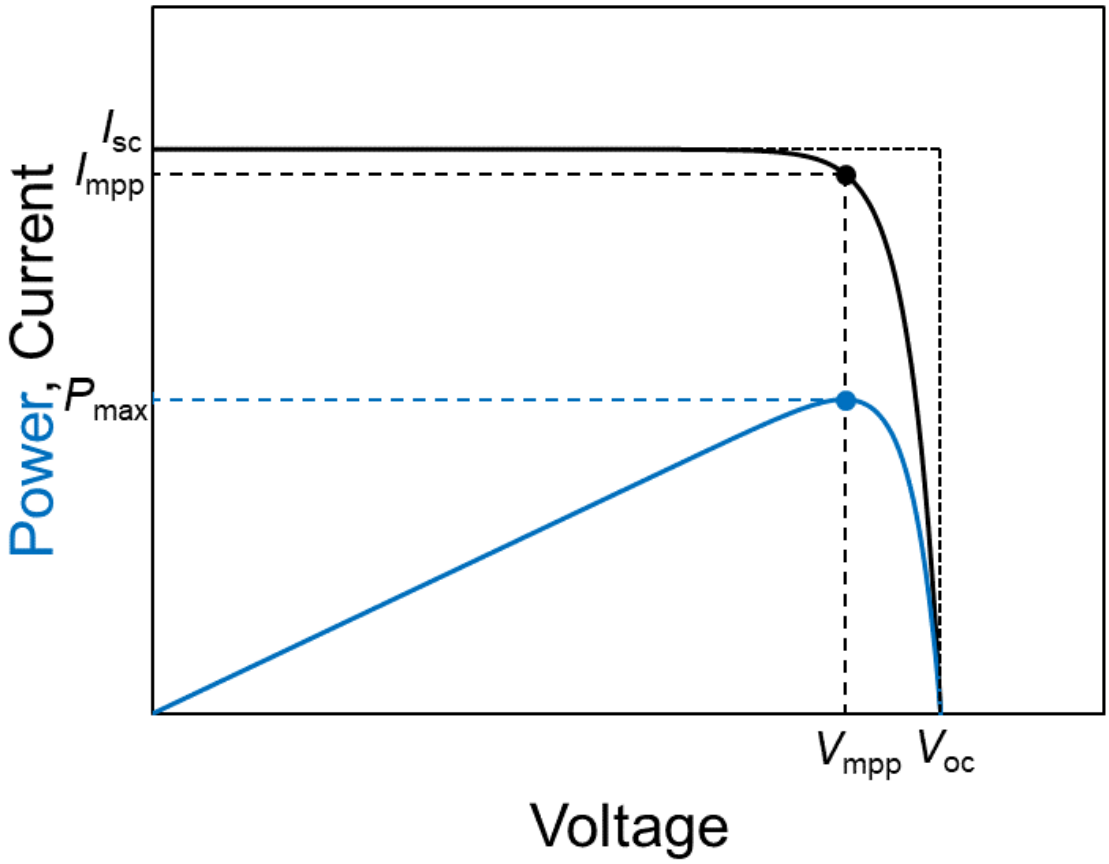

Figure 2.3: Ideal solar cell current-voltage (I-V) and power curves. I_{sc}: short-circuit current, I_{mpp}: current at maximum power point, P_{max}: maximum power, V_{oc}: open-circuit voltage, V_{mpp}: voltage at maximum power point.

The fill factor is a ratio of the maximum power, and the product of I_{sc} and V_{oc}:

$$FF = \frac{P_{max}}{I_{sc}V_{oc}} = \frac{I_{mpp}V_{mpp}}{I_{sc}V_{oc}} \tag{21}$$

It can be interpreted as a ratio of the rectangles given by $I_{mpp}V_{mpp}$ and by $I_{sc}V_{oc}$, as shown in Figure 2.3. A higher fill factor indicates less losses and higher conversion efficiency. The conversion efficiency, η, is a ratio of the maximum power out and the incident power from light on the cell, P_{in} given by:

$$\eta = \frac{P_{max}}{P_{in}} = \frac{I_{mpp}V_{mpp}}{P_{in}} = \frac{I_{sc}V_{oc}FF}{P_{in}} \tag{22}$$

Losses in the solar cell can be modeled as two parasitic resistances: a series resistance, R_s, and a shunt resistance, R_{sh}. The series resistance accounts for resistance in and between components of the cell including metal contacts and any other resistances along the current's desired

pathway. The shunt resistance accounts for any alternative current pathways including defect-assisted recombination and edge shunting. They are added to the solar cell equivalent circuit in Figure 2.4.

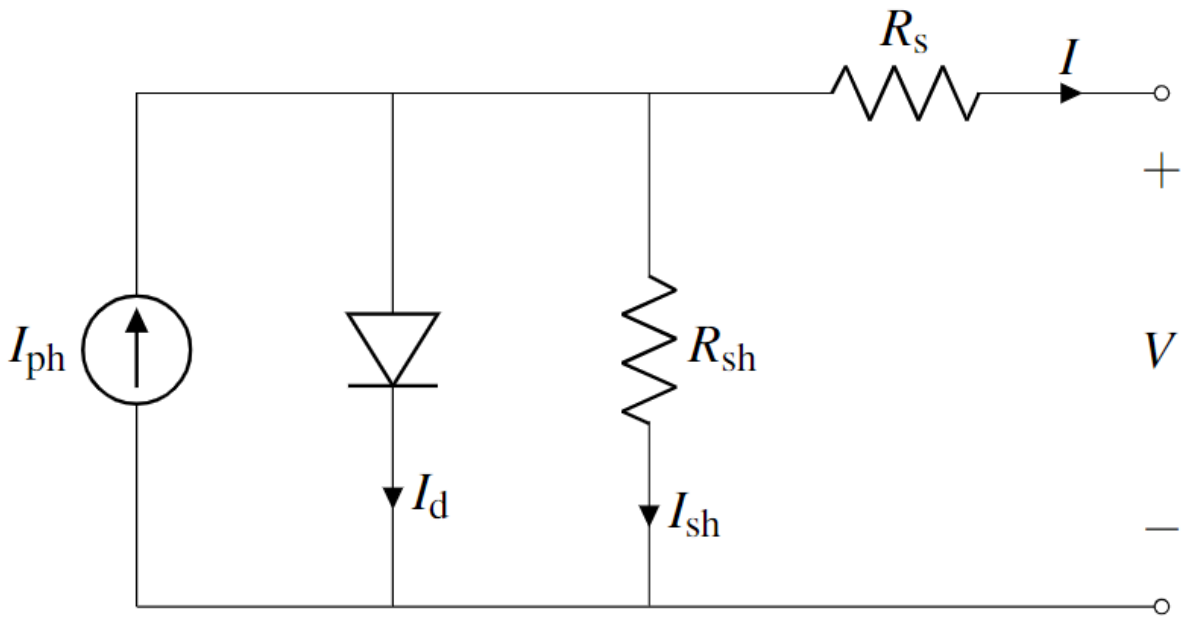

Figure 2.4: Solar Cell equivalent circuit with series and shunt resistances.

Applying Kirchhoff's current law to Figure 2.4 yields:

$$I = I_{ph} - I_0 \left(e^{\frac{q(V+IR_s)}{kT}} - 1 \right) - \frac{V + IR_s}{R_{sh}} \tag{23}$$

where I is the current, I_{ph} is the photogenerated current, and I_0 is the diode saturation current. As shown in Figure 2.5, the parasitic resistances decrease the FF. The nonzero series resistance pushes the V_{mpp} further from the V_{oc}, and is more significant at high current. The finite shunt resistance pushes the I_{mpp} further from the I_{sc}, and is more significant at low current. If the series resistance is too high, or shunt resistance too low, the cell will operate as a resistor.

2.1.6 Photovoltaic Modules and Systems

Solar cells are often packaged side-by-side in a module with some combination of series and parallel electrical connections. The combination of series and parallel connections within a module is a trade-off between cost, performance, and practicality. To reduce I^2R power losses in connecting wires and to make the module compatible with the voltages of batteries and other

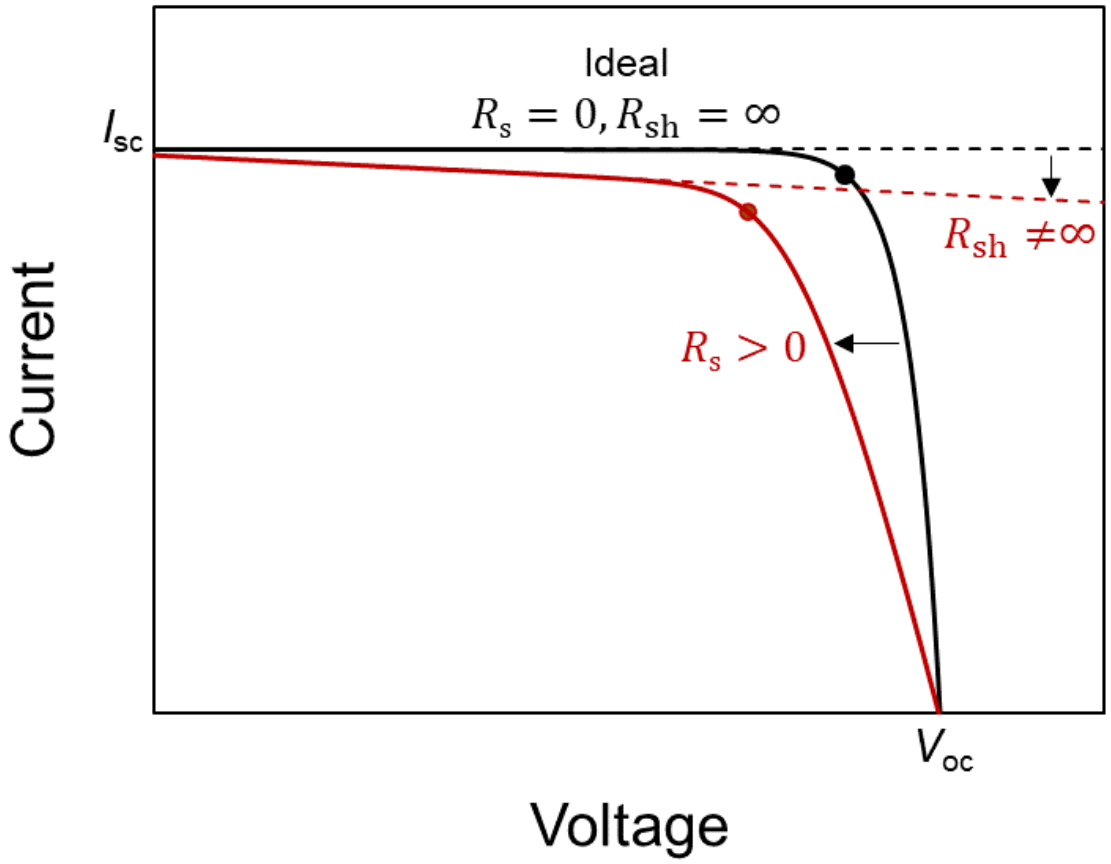

Figure 2.5: Solar cell current-voltage (I-V) curve with series and shunt parasitic resistances compared to an ideal curve with $R_s = 0$ and $R_{sh} \neq \infty$.

interconnections, cells are first strung in series to increase voltage. However, if two or more series-connected cells receive different amounts of incident light, the current of all the cells in the series will be limited by the cell receiving the least light, i.e., generating the least current. Shading on solar modules should therefore be avoided because it leads to both direct losses due to less incident light generating less current, and indirect losses due to the resulting electrical mismatch. The drop in voltage due to a single shaded cell can be significant if left unaddressed and can lead to irreversible damage to the module due to hot-spots from the power dissipated in the shaded cell [41].

Current losses between series connections and hot-spots are mitigated by connecting a bypass diode in parallel with opposite polarity as the solar cell equivalent diode. Bypass diodes provide an alternate current pathway for shaded or otherwise under performing cells and limits the

voltage drop across the cell to that of the bypass diode. However, it is expensive and impractical to include a bypass diode between each cell. Instead, one to three bypass diodes are often used per module to connect a group of series-connected cells in parallel, forming a submodule, to mitigate electrical mismatch losses.

Similar to solar cells, solar modules are wired in series to increase voltage, and parallel to increase current. A group of modules strung in series are known as a string of modules, and the entire collection of modules at a location is known as a solar array or system. The modules are first strung in series up to the desired voltage of the system to mediate I^2R power losses in connecting wires, and then parallel connections are added to increase current and maximize the power of the system.

Losses between parallel connections in an array are mitigated with blocking, or isolation, diodes placed at the end of each string. The blocking diodes prevent shaded, malfunctioning, or under performing strings from drawing reverse current. It is therefore crucial to design solar systems with uniform illumination between strings.

Tracking systems can maximize the illuminated cross-sectional area of modules by rotating the modules throughout the day, reducing cosine and angle of incidence losses as well. At high sun zenith angles, trackers mitigate shading between strings by tilting towards horizontal, in a process known as backtracking. Two-axis trackers always face the sun directly by tracking its azimuth and zenith angles. Single-axis trackers follow one of the angles using one of four approaches: horizontal, i.e., parallel to the ground, with north-south axis rotation; horizontal east-west axis rotation; tilted modules facing the equator rotated about a vertical axis; and rotation about a polar axis with tilt angle equal to the latitude at the site location. This work includes module-level results for horizontal single-axis trackers with north-south axis rotation, i.e., rotating modules from east to west throughout the day. Tracking rotation is achieved with a TT that spans the length of several adjacent modules, forming a row.

2.2 Bifacial Photovoltaics

Conventional solar cells are monofacial and absorb light only through their front face. Bifacial solar cells absorb light through both the front and rear faces. This leads to increased energy yield; especially in high diffuse light conditions and in cases with high albedo. With monofacial and bifacial modules sharing many fabrication techniques, bifacial modules produce more energy at a similar cost, driving down the levelized cost of energy of bifacial systems. Single-

axis tracking systems can further increase yield and reduce the levelized cost of energy. As a result, the bifacial PV market share is expected to grow considerably from 50% in 2021 to 85% in 2032 [3].

The gain in energy yield that bifacial cells or modules have over monofacial cells or modules is defined as:

$$\text{Bifacial Gain} = \frac{EY_{\text{bi}} - EY_{\text{mono}}}{EY_{\text{mono}}} \tag{24}$$

where EY_{bi} is the energy yield of a bifacial cell or module, and EY_{mono} is the energy yield of an equivalent monofacial cell or module. Bifacial installations can have bifacial gains up to 30% depending on a complex set of factors including the tracking system, ratio of diffuse and direct light at the site's location, the ground albedo, and racking structure [6], [42].

Significant strides have been taken to increase accuracy in bifacial PV energy yield predictions and hasten the adoption of bifacial PV including comparisons between software [4], [5], and validation against field data [6]–[13]. However, the bifacial PV market is still maturing, and uncertainty in energy yield prediction can hinder system design and their adoption over alternative investments [14]. In addition to accurately modeling the front and rear incident irradiance, bifacial PV energy yield prediction tools must quantify the electrical mismatch. PV modules are subject to electrical mismatch from varying cell maximum power points due to manufacturing tolerances, temperature gradients, and irradiance nonuniformity stemming from many factors including object shading, passing clouds, soiling, and proximity to the ground [32], [41], [43]. In particular, racking elements in bifacial PV systems introduce shading and reflections on the rear face, increasing rear irradiance nonuniformity and electrical mismatch [15]. The effects of racking, particularly from the TT in single-axis trackers as it spans the middle of the rear collector surface, must be accurately quantified in energy yield predictions to further reduce investor risk, increase stakeholder confidence, and hasten the adoption of tracked bifacial PV [14].

Ray tracing bifacial PV performance modeling software [6], [11]–[13], [17]–[20] can model shading and reflections from racking elements at a high computational cost by simulating many stochastic rays interacting with multiple textured surfaces. 2D [7]–[9], [21]–[26] and 3D view factor models [27]–[31] either estimate racking shading with user-defined shading factors determined by comparing PV performance with and without racking [22]–[25], or account for racking shading using simulations of instantaneous ray-object intersection [26]. Hybrid modeling software employ a view factor method for the front irradiance only [5]. One possible enhancement of 3D view factor models with detailed shading accounted for using ray-object intersection is the inclusion of racking reflections, specifically from the TT. However, the isolated impact of racking reflections on PV performance is not well documented.

McIntosh et al. showed that the relative reduction in module power due to nonuniform illumination, including racking shading, is greatest at solar noon in sunny conditions, and greater for 1P than 2P single-axis tracker frameless modules, decreasing central module yield by 0.23% and 0.09% respectively [15]. However, the racking reflection's contribution was not isolated. Deline et al. found annual mismatch losses of less than 0.5% for 1P single-axis tracked systems [32]. Guerrero Pérez et al. showed, for a sunny summer day, the rear insolation in a 2P single-axis tracker decreased by 12% with an absorptive TT but only 1.3% with a reflective TT [33].

In Chapter 3 we extend previous work to compare the irradiance impact of TT reflection in both 1P and 2P trackers. Including a reflective TT surface rather than a fully absorptive surface increases annual rear insolation by 3% and 5.5% for modules on 1P and 2P single-axis trackers, respectively. In Chapter 4 we quantify the impact of TT reflection on irradiance, electrical mismatch, and total energy yield based on sun position and sky condition using a hybrid modeling approach with a ray tracing model, bifacial_radiance [11], [17], [18] to extract the TT reflection. We introduce this reflection as an additional irradiance source in DUET [31], a 3D view factor model with detailed shading, to assess the impact of TT reflection in such a model. Using DUET, we can also include and quantify the impact of an incidence angle modifier on the TT reflection's contribution to energy yield. Isolating the TT reflection and accounting for angle of incidence losses was not possible with either simulation method alone, thus bifacial_radiance and DUET were appropriate for this work.

2.3 bifacial_radiance

bifacial_radiance is an open-source toolkit by the US National Renewable Energy Laboratory (NREL) for simulating the performance of bifacial PV modules and systems [11], [17], [18]. It is built around and facilitates the use of the ray tracing software RADIANCE which predicts illumination in designed spaces.

The bifacial_radiance application programming interface (API) is implemented in three layers: core functions that provide text commands directly to RADIANCE; a layer of abstraction with classes that provide methods to communicate with RADIANCE more effectively; and a final layer including the graphical user interface, and a class designed to simplify the process of simulating a PV system over a time series of weather data by stitching together many of the modeling steps. The middle layer of abstraction calculates solar position from meteorological data using algorithms from pvlib [44], links the sky information to PV module objects and other nearby objects when calling the core RADIANCE functions, then analyzes and returns results

to the user.

Ray tracing models simulate many stochastic rays that interact with multiple textured surfaces. This allows the user to reproduce complex PV systems, including shading, reflections, and finite-system edge effects. Conventional ray tracing creates many stochastic rays originating from the light source(s) and traces them to their eventual target. This can produce realistic lighting environments, however, the main area of interest in PV modeling is the irradiance incident on the module. We don't need to use computational resources to reproduce the light around the module. Therefore, bifacial_radiance benefits from RADIANCE employing reverse ray tracing instead of conventional ray tracing. In reverse ray tracing, many stochastic rays originate from the area under investigation and are computed towards the incident irradiance only if they trace back to a light source.

2.3.1 RADIANCE

RADIANCE is an open-source suite of programs for analyzing lighting in a space. It was developed by the Lighting Systems Research group at Lawrence Berkeley Laboratory by Greg Ward [45], [46].

Inputs include 3D geometric models, materials, light emitters, time, date, and sky conditions. Additional inputs are required for rendering an image including the location of the viewpoint, the direction, and the angles, however this is not necessary for bifacial_radiance. The lighting simulation engine uses a hybrid approach of Monte Carlo and deterministic, i.e., reverse, ray tracing to calculate the spectral radiance, irradiance, and glare indices. Spectral irradiance is the light emitted, passing through or reflected from a surface. Irradiance is light falling onto a surface. Glare indices are the degree of brightening from direct or reflected light used when rendering a particular viewpoint. The resulting map of spectral radiance values and other derived radiometric quantities may be output as numerical data (which bifacial_radiance uses), contour plots, or displayed as colour images.

There are three main steps to using RADIANCE: 1) specify the physical environment, known as the scene, as simple geometric elements such as polygons, spheres, rings, cylinders, or cones that can be interpreted by RADIANCE; 2) assign each geometric element a material or property and specify light sources; and 3) render the scene to produce an image. Rendering a scene optional for bifacial_radiance computations. In practice, the first two steps are done simultaneously because every object must be assigned at least one material.

Specifying 3D geometry and material properties encompass scene description and is accomplished with text files. Geometry may be imported from a 3D computer-aided design (CAD) system with help from a conversion program or specified using RADIANCE textual inputs, known as primitives. The material of an object is described using RADIANCE primitives and determines how light interacts with the surfaces. All scene description primitives have the following format:

optional comment ending with a return

modifier type identifier

n A number (n) of string arguments

Ø A number (Ø) of integer arguments (not used in RADIANCE)

m A number (m) of real number arguments

The identifier is the label the user gives the primitive, the type is one of RADIANCE's base primitives, and the modifier must be either a previously defined primitive or the word void when the primitive does not need to be modified. Any line starting with an exclamation point is executed, and the output is read as input to the RADIANCE calculation.

```
#  Blue material definition
void  plastic  Blue_mat
Ø
Ø
5  Ø  Ø  1  Ø  Ø
```

Blue_mat is the identifier of the newly defined primitive, and void indicates that no modifier is applied to the RADIANCE base primitive, plastic. The next two lines are zero because there are no string or integer arguments for the plastic primitive. Finally, the last line starts with 5 to indicate there will be 5 real numbers of input to follow. In this case for the plastic primitive, the last five numbers specify the material red, green and blue (RGB) colour reflectance (Ø Ø 1), the specularity (Ø) and the roughness (Ø). The plastic primitive inputs all range from zero to one. RGB reflectance varies from 0, fully absorptive, to 1, fully reflective. Specularity varies from 0, fully diffuse reflection, to 1, fully specular reflection. Finally, roughness varies from 0, planar reflection, to 1, fully random reflection. There is a distinction between specularity and

roughness because RADIANCE calculates direct, specular indirect, and diffuse indirect light separately. Specifying all the RADIANCE base primitives is beyond the scope of this work, but more information can be found here [46].

Continuing the example, the following text uses Blue_mat to specify a blue sphere:

```
#    Blue sphere labelled ball

Blue_mat    sphere    ball

Ø

Ø

4    Ø    Ø    Ø    2
```

Blue_mat modifies the sphere base primitive to specify a sphere labelled ball that has a material given by Blue_mat. The next two lines are again zero because there are no string or integer inputs for the sphere primitive. The last line indicates there will be 4 real numbers of input to follow. In this case for the sphere primitive, they specify the center position (Ø Ø Ø), and radius (2).

The main advantage of using RADIANCE over other lighting calculation tools is there are few limitations on the geometry or materials that may be simulated. In particular, the material may be specified as one of or any combination of the following four classes of materials: normal, such as plastic, metal, transparent, or mirrors which all reflect and/or transmit light; lights, which emit light; dielectrics, which refract and reflect light with a specified index of refraction; and bidirectional reflectance transmittance distribution function materials, which offer the user more flexibility in setting diffuse and specular surface reflectance and transmittance but should be used with great care to produce a physically valid reflection model. Outside of the sky dome, normal materials are the only materials used to describe RADIANCE scene objects in this work.

Once a scene has been described, it is compiled into a data structure called an octree to enable ray tracing. An octree is a tree data structure often used to divide a 3D space. Each node of an octree has exactly eight children which recursively subdivide the space into eight octants around a point. The subdivision stopping point can be determined by reaching a maximum number of subdivisions, by attaining a minimum octant size, or by an octant containing fewer than a given number of points. Octrees use a depth-first search in which each branch is explored as far as possible before backtracking so that only required surfaces are viewed. This is the fundamental system enabling reverse ray tracing.

RADIANCE's octree starts with a cube encompassing the entire scene and recursively subdivides the cube until each child intersects or contains less than a set number of surfaces or reaches a certain size. At each surface point, RADIANCE recursively evaluates the reflected radiance (SI units of $\mathrm{Wsr}^{-1}\mathrm{m}^{-2}$) in a specific direction,

$$L_r(\theta_r,\phi_r) = L_e(\theta_r,\phi_r) + \int_0^{2\pi}\int_0^{\pi/2} L_i(\theta_i,\phi_i)\rho_{bd}(\theta_i,\phi_i;\theta_r,\phi_r)|\cos\theta_i|\sin\theta_i d\theta_i d\phi_i \tag{25}$$

where θ is the polar angle measured from the surface normal, ϕ is the azimuthal angle measured about the surface normal, $L_e(\theta_i,\phi_i)$ is the emitted radiance, $L_i(\theta_i,\phi_i)$ is the incident radiance, and $\rho_{bd}(\theta_i,\phi_i;\theta_r,\phi_r)$ is the bidirectional reflectance-transmittance distribution function in sr^{-1} [47]. Wavelength and polarization of light are left out of the equation for simplicity but are contained implicitly in ρ_{bd}. This uses Kajiya's rendering equation 1 in [48] but replaces the notion of energy transfer between two points with the energy passing through a specific direction.

The calculation can be divided into three separate light components calculated in the following order: direct, specular indirect, and diffuse indirect. Direct light includes both light arriving at a surface directly from a source, and light reflected from or transmitted through a perfectly specular surface. Specular indirect light includes light arriving at a surface from another non-emitting source that is not perfectly specular, including reflected light or refracted light. Diffuse indirect light includes light arriving at a surface from a reflection or transmission with no directional preference.

The ray direction and intensity of each light component is determined in the following ways. Interactions with perfect specular surfaces simply redirect the ray based on the incident angle and the surface normal. Imperfect specular surfaces use Monte Carlo sampling to determine specular indirect light. Finally, the diffuse indirect light component takes advantage of its small variation over a surface by interpolating values from a few Monte Carlo calculations taken at carefully spaced locations, with more samples placed in areas with large light gradients to improve accuracy [49], enhanced by gradient information [50]. This interpolation cuts down on the number of computationally expensive diffuse indirect light Monte Carlo estimations which require the examination of hundreds of ray directions due to the nature of the light.

In addition to interpolating samples of diffuse indirect light RADIANCE uses more techniques to reduce computational intensity and improve accuracy. Light sources that are large relative to their distance from a sampled surface are adaptively subdivided until each subsection of the light source meets a desired size and distance ratio [51]. In addition, RADIANCE sends out

a few "pre-sampling" rays to help minimize the number of required rays. The pre-sampling rays help determine if the system should introduce a virtual light source to help calculate light reflecting off a specular surface onto a diffuse or semi-specular surface. These virtual light sources replace a light source for rays reflecting off a specular surface but are placed such that it appears as though the light were transmitted through the specular surface. The benefit is that ray tracing is now calculated directly from the sample to the virtual light source instead of from the sample to the specular surface and then to the light source. The pre-sampling rays also sort the light sources in a scene based on their potential contribution and model each source in that order, keeping track of the number of unobstructed rays to the light source and shaded rays. Once a threshold percentage of the light on the surface has been accounted for, the remaining light sources can be approximated with the same fraction of shadow rays or carried out in full for a more rigorous lighting evaluation. This technique is useful for modeling scenes with many light sources but is not required or used in bifacial_radiance because most PV systems have a single small light source in the sky, and the most accurate calculation possible is desired.

Finally, instead of relying on random samples over the hemisphere, RADIANCE sends a single sample ray towards the sun, and if it arrives unobstructed, it uses a deterministic calculation of the total solar contribution based on the known size and luminosity of the sun.

2.4 DUET

DUET is the University of Ottawa SUNLAB's python-based numerical performance software for bifacial PV with integrated optical and electrical models [31], [52], [53]. DUET calculates irradiance profiles and energy yield for each hourly or sub-hourly timestamp in an input weather file given PV array geometry (fixed-tilt or single-axis tracking, racking dimensions, row-to-row spacing, ground clearance, etc.), and module electrical parameters. The optical model builds on a 3D view-factor approach by accounting for shading from objects in the scene using simulations of instantaneous ray-object intersection. It produces 2D front and rear irradiance profiles with shading from racking or other objects in the scene for a specified module under investigation in the PV array. The electrical model calculates the $I-V$ curve of each cell and quantifies electrical mismatch loses from irradiance nonuniformity. Multiple modules can be simulated to generate $I-V$ curves for strings of modules and entire arrays.

The optical model calculates irradiance from three sources: direct solar radiation, anisotropic diffuse sky dome radiation, and reflected radiation from the ground. The diffuse sky dome, ground, and module front and rear under test are separated into patches. The irradiance on each

module patch is the sum of the irradiance from all sources including direct beam, from each sky patch, and from each ground patch. The energy transfer between patches depends on the area of the irradiated patch, the angle of incidence, and the solid angle between the irradiated and emitting patches. In addition, a shading object in the array between two patch centroids can partially or completely block light transfer between patches. All shading objects in DUET are considered absorptive, thus DUET alone does not capture reflections off racking elements. The only reflective surface is the ground, making all rays deterministic and independent, and allowing for computational efficiency improvements through parallel processing and vectorization. The ground patches assume Lambertian reflection, with equal intensity in all directions, and is spectrally flat.

The radiation from each patch in the diffuse sky dome is found with the 1993 Perez anisotropic sky model [54]. The model determines sky clearness and brightness from direct normal irradiance (DNI) and diffuse horizontal irradiance (DHI), then generates a normalized radiation distribution scaled by each timestamp's DHI and accounting for sun position. When the sun is below the horizon, the the diffuse sky dome is isotropic.

The electrical model calculates the $I-V$ curve of each cell at each timestamp using a cell temperature dependent single-diode model. In bifacial energy yield calculations, the rear-side irradiance is de-rated by a bifaciality factor which accounts for the decreased probability of carrier collection from rear-incident light, and then it is added to the front-side irradiance. The module $I-V$ curve is determined by combining all cell $I-V$ curves depending on the user-specified module wiring architecture. The module's instantaneous power is then multiplied by the timestamp duration to find the total energy yield.

Chapter 3: Torque Tube Reflection Irradiance

3.1 Preface and Author Contributions

This chapter presents our Photonics West 2022 proceeding, which was published through SPIE on March 4, 2022. The work quantifies the impact of incorporating a reflective TT on rear insolation, the time integrated irradiance equivalent, and rear insolation mismatch for 1P and 2P bifacial modules on horizontal single-axis trackers over an hourly typical meteorological year in Livermore, California, USA provided by the NSRDB [34]. At the time of simulation, bifacial_radiance did not offer features such as including frames on modules, or 2D irradiance sampling of the module(s) under test necessary for determining the irradiance near module edges. These features were implemented by the lead author and are described in the publication below. Simulations, analysis, and lead writing was performed by T. J. Coathup. Contributions from authors: M. R. Lewis, advice, writing, and edits; A. C. J. Russell, advice, and writing; A. Conesa, conceptualization; J. Guerrero-Perez, conceptualization; C. E. Valdivia, advice, and writing; K. Hinzer, conceptualization and writing.

3.2 Publication - Photonics West 2022

Trevor J. Coathup, Mandy R. Lewis, Annie C. J. Russell, Alejandro Conesa, Javier Guerrero-Perez, Christopher E. Valdivia, Karin Hinzer, "Impact of reflective torque tube on rear side irradiance in bifacial photovoltaic modules," Proc. SPIE 11996, Physics, Simulation, and Photonic Engineering of Photovoltaic Devices XI, 119960A (4 March 2022); doi: 10.1117/12.2615658.

Impact of reflective torque tube on rear side irradiance in bifacial photovoltaic modules

Trevor J. Coathup[a], Mandy R. Lewis[a], Annie C. J. Russell[a], Alejandro Conesa[b], Javier Guerrero-Perez[b], Christopher E. Valdivia[a], Karin Hinzer[a]
[a]SUNLAB, Centre for Research in Photonics, University of Ottawa, Ottawa, ON, Canada
[b]Soltec Innovations, Murcia, Spain

ABSTRACT

Non-uniform irradiance on the rear side of bifacial photovoltaic (PV) modules causes electrical mismatch between cells and energy loss across the module. Racking structures increase this non-uniformity through shadows and reflections that vary throughout the day. However, commercial software typically use constant values to estimate mismatch losses in annual simulations.

We investigate the impact of torque tube shading and reflection on rear side irradiance mismatch in bifacial PV modules in one-in-portrait (1P) and two-in-portrait (2P) horizontal single-axis trackers with a range of ground albedos over a typical meteorological year in Livermore, California, USA. Irradiance simulations use a version of bifacial_radiance, the National Renewable Energy Laboratory's python wrapper for the RADIANCE ray tracing software, which we modified for arbitrary 2D irradiance sampling of the module(s) under investigation.

For a torque tube reflectivity of 0.745, torque tube reflection accounts for 3.0% and 5.5% of the annual rear insolation in 1P and 2P configurations, respectively, for a 0.2 albedo; or 2.9% and 3.1% for a 0.6 albedo. Torque tube reflection decreases annual rear insolation mismatch from 11.8% to 10.7% in 1P configurations, and from 11.5% to 9.8% in 2P configurations with 0.2 albedo. Similarly, with 0.6 albedo, annual rear insolation mismatch decreases from 12.6% to 11.6% in 1P configurations, and from 11.9% to 10.4% in 2P configurations. However, we demonstrate that annual figures are insufficient for capturing the impact of torque tube reflection; seasonal and diurnal variations must also be considered.

Keywords: Annual energy yield modelling, ray tracing, single axis tracking, silicon module, rear shading, global irradiance, ground albedo, PV system racking

1. INTRODUCTION

Bifacial photovoltaics (PV) are becoming an increasingly important segment of the silicon photovoltaics industry, with bifacial PV predicted to make up 80% of the market share within the next ten years [1]. Single-axis tracking (SAT) systems can further increase energy yield by rotating the modules throughout the day, typically from east to west, thereby maximizing illuminated cross-sectional area, and reducing cosine and angle-of-incidence losses [2]. Pairing these two technologies can reduce the levelized cost of energy (LCOE), improving the cost-competitiveness of bifacial PV [3]. To hasten the adoption of these technologies across a wider range of deployment conditions and system configurations, accurate energy yield predictions are essential to reduce investment risk and increase investor confidence [4]. However, bifacial energy yield models are still undergoing development and validation, and their uncertainty may act as a barrier to adoption [4].

One of the challenges of bifacial PV performance modelling is accurately accounting for the effects of racking elements on the rear irradiance. Most SAT systems have rows of PV modules rotating around a torque tube (TT) that runs the length of the row, but the system configuration can impact rear irradiance and, as a result, energy yield. For example, SAT two-in-portrait (2P) modules, where one module is mounted on each side of the torque tube, show higher bifacial gain than one-in-portrait (1P) modules, where the torque tube runs behind the center of the single module [5]. Some optical models, such as ray tracing models, can represent mounting structures and account for light blocked or reflected by the torque tube on specific parts of the PV module. However, it is more common for simplified bifacial PV performance models to

represent racking shading by a constant rear shading factor applied to reduce the total energy yield at the end of the calculation [6]. Torque tube shading can cause reduced and non-uniform irradiance leading to increased electrical mismatch and reduced total energy yield output [7]–[9]. In addition, constant shading factors applied to bifacial PV performance models do not typically account for light that is reflected from the torque tube. Torque-tube-reflected light can increase rear-side irradiance, and consequently energy yield, with approximately 1% electrical mismatch loss [9]. The isolated impact of torque tube reflection on rear irradiance mismatch is not widely reported in the literature.

In this work, we model the central module rear-side irradiance of comparable 1P and 2P North-South horizontal SAT bifacial systems. For modules in 1P and 2P configurations, we quantify the impact of torque tube reflection on the rear irradiance magnitude, 2D profile, and mismatch at 0.2 and 0.6 ground albedo. First, we will describe the model and system configuration. Next, we will outline trends in torque-tube-reflected irradiance on a summer and winter day. Finally, we will show annual effects of torque tube reflection based on time of day and month of year.

2. MODEL DESCRIPTION

The PV systems were modelled in bifacial_radiance [10]–[13], an open-source software by the National Renewable Energy Laboratory (NREL) built around RADIANCE [14], a ray tracing software. For this study, the following modifications were made to bifacial_radiance (version 0.3.4): (1) adjustments to the ray trace settings to improve accuracy, particularly at the module edges near the frame where shading is high; (2) the addition of module frames and module supports to the module under test (Figure 1a, Figure 1b); (3) the removal of torque tube objects from rows not under test; and (4) the implementation of 2D irradiance sampling on the module under test.

In bifacial_radiance, there are two accuracy settings included by default (low and high) that set the parameters for RADIANCE's ray trace method, *rtrace* [15]. The high accuracy method has a longer runtime but results in less noise in the irradiance data than the low accuracy method. In this work, each irradiance value was calculated multiple times (3 times for annual simulations and 10 times for select days), then averaged to reduce the noise. Additionally, the *rtrace* ambient accuracy parameter, *aa*, was altered from the default bifacial_radiance low accuracy option of 0.1 to 0.05 to improve the calculation's accuracy with minimal increase to the computation time.

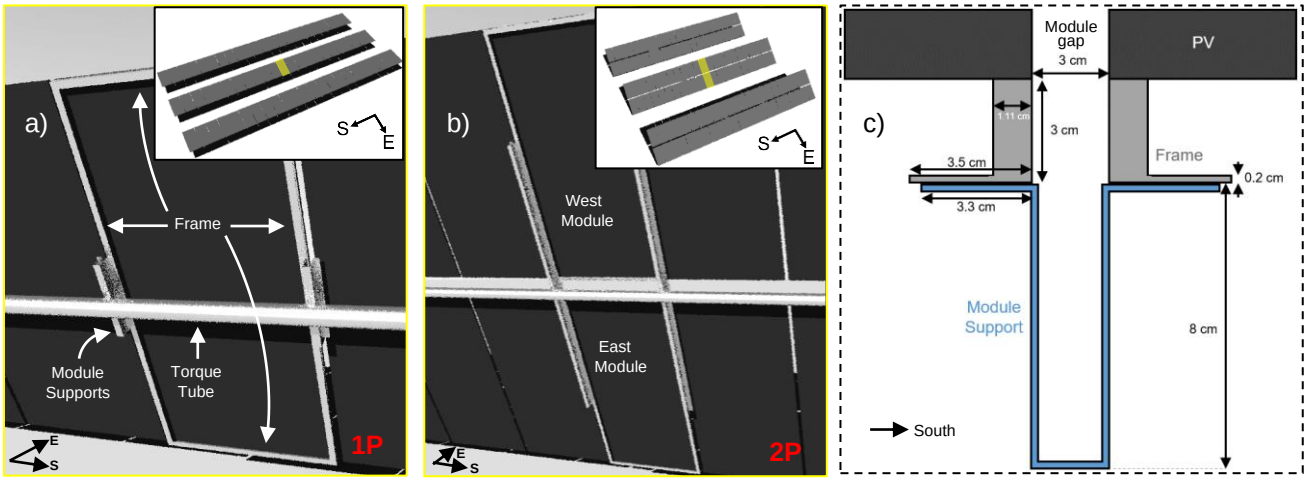

Figure 1. Module supports and frame on the module under test for (a) 1P and (b) 2P modules with a reflective torque tube along the row under test. Overview of the modelled 3 row by 23 module 1P array (a-inset) and 2P array (b-inset) with the central module(s) highlighted. Cross-sectional schematic (c) shows the frame and module support dimensions common for both 1P and 2P looking down the length of the module. Frame dimensions are the same along each of the module edges.

We calculated rear irradiances for the center module(s) of both a 1P and a 2P horizontal SAT system from hourly Typical Meteorological Year (TMY) data for the Bifacial Test Evaluation Center (BiTEC) site in Livermore, California, USA (37.70° N, 121.82° W, 121 m elevation). The scene parameters for the modelled 1P and 2P systems are presented in Table 1. Parameters were chosen to emulate a Soltec 2P tracker and a comparable 1P configuration [16], but with a round torque tube shape rather than square. The 1P system consisted of 3 rows of 23 modules (Figure 1a inset), while the 2P system consisted of 3 rows of 23 sets of 2 side-by-side modules (Figure 1b inset), with the torque tube oriented north-south and parallel to the ground in both systems. Piles were not included in the array geometry because each module is affected differently by pile shading due to their proximity to or distance from a pile. Omitting piles allows the single-module results to be interpreted more generally.

Rather than including a module frame and module supports on every module in the test array, these elements were only included on the module under test, as shown in Figure 1a and b, to decrease computation time. Similarly, the torque tube was only included for the row with the module under test. Detailed frame and module support dimensions are illustrated in Figure 1c. The module supports were positioned between, and directly in contact with, the torque tube and module frame. In single-timestamp benchmarking tests, these simplifications decreased computation time by approximately a factor of 10, while changing total torque-tube-reflected irradiance by 2.6% absolute.

Table 1. Scene parameters used in bifacial_radiance for the 1P and 2P systems.

Scene Parameter	**1P System**	**2P System**
System configuration:		
Modules per row	23	23
Number of rows	3	3
Row pitch	4.8355 m	10 m
Ground cover ratio	0.456	0.456
Piles	Not included	Not included
Ground clearance	1.35 m	2.35 m
Tracking angle range	±60°	±60°
Site configuration:		
Location	Livermore, CA	Livermore, CA
Irradiance data	TMY	TMY
Albedo	0.2 & 0.6	0.2 & 0.6
Module:		
Width	1.032 m	1.032 m
Length	2.205 m	2.205 m
Thickness	0.02 m	0.02 m
Module gap	0.03 m	0.03 m
Module supports:		
Height	0.08 m	0.08 m
Length	0.44 m	2.8 m
Width	0.03 m	0.03 m
Torque tube:		
Torque tube gap	N/A	0.15 m
Shape	Round	Round
Diameter	0.1 m	0.1 m
Reflectivity	0.745 | 0	0.745 | 0
Specularity	0.9	0.9
Roughness	0.2	0.2

Module dimensions emulate the Jinko Solar Tiger Bifacial JKM460M-7Rl3-TV module [17]. They are set as 1.032 m wide and 2.205 m long, with a 0.03 m gap between modules, and a 0.15 m gap between the 2P east and west modules. The row-to-row pitch is set to maintain a ground ratio coverage (GCR) of 0.456: 10 m for the 2P system and 4.8355 m for the 1P system. GCR is defined as a ratio of the collector length to the row-to-row pitch, where the collector length is the width of the module row (including east and west modules and the module gap in the 2P case) [9]. The collector tilt angle is controlled by PVLib's tracking algorithm [18], with a maximum tracking angle of ±60° and backtracking enabled.

To isolate and study torque tube reflection, the rear irradiance of the module under investigation is first sampled in a 2D array of 52x24 points per module face (1248 for 1P, 2496 for 2P) with a reflective torque tube, as shown in Figure 2a. We set the reflective torque tube material to a reflectivity of 0.745, specularity of 0.9, and roughness of 0.2. The module support and module frame were modelled with the same material parameters as the reflective torque tube. The high number of sampling points captures the irradiance and irradiance mismatch effects near the module edges and racking fixtures including the frame, module supports, and torque tube. Next, the simulation is repeated with the torque tube reflectivity set to 0, as shown in Figure 2b. The module support and module frame materials remain reflective in the absorptive torque tube case. The difference between the rear irradiance with a reflective torque tube and the rear irradiance with a fully absorptive torque tube yields the torque tube reflection signal, shown in Figure 2c. While these figures illustrate the 2P rear irradiance values of a single timestamp at noon on a summer sunny day (June 19) with 0.2 ground albedo, the process is identical for each timestamp and albedo, as well as for the 1P module.

Figure 2c shows the torque tube reflection is predominant near the torque tube, and is relatively flat along the North-South direction, illustrated by the cross-sectional averages along the module width (Figure 2d) and along the collector width (Figure 2e). The torque tube reflection profile is only impacted by the frame at the edge nearest the torque tube, even though the frame reduces the total irradiance (Figure 2a and b) throughout the entire perimeter of the modules.

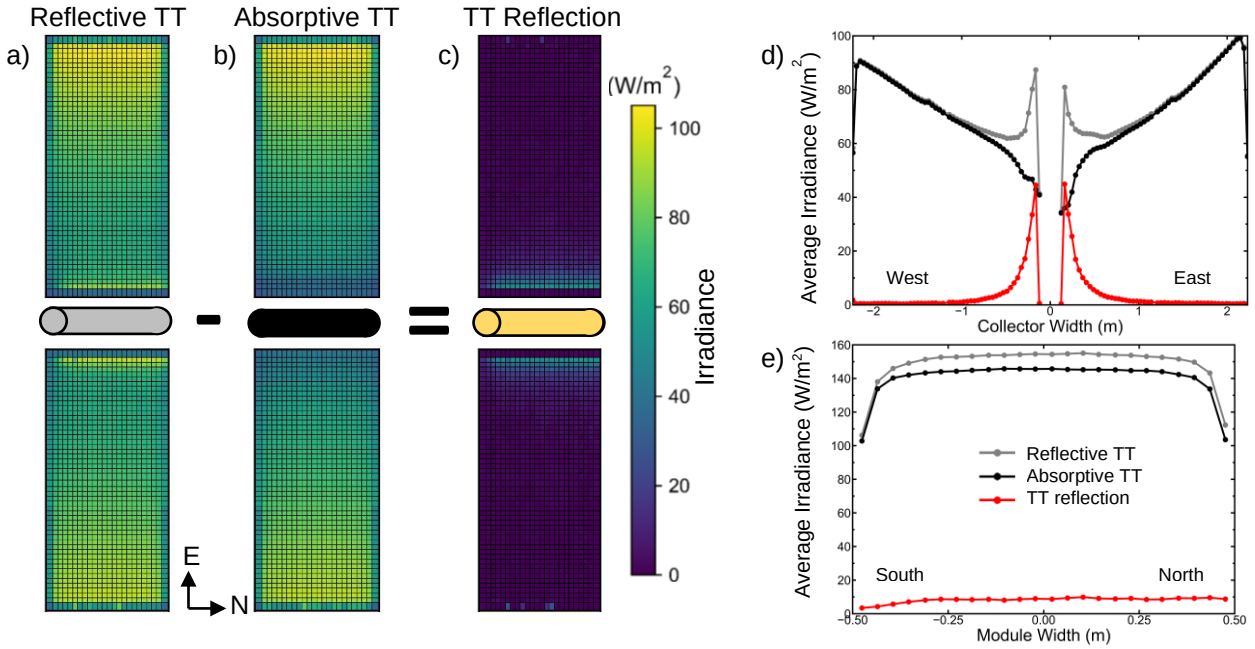

Figure 2. Torque tube (TT) reflection calculation procedure illustrated by 2P rear irradiance values from noon on a summer sunny day. 2D irradiance map of the rear face of the module with (a) a reflective torque tube and (b) an absorbing torque tube. Subtracting (b) from (a) yields (c), a 2D irradiance map of the torque tube reflection. The irradiance averaged along (d) the module width and (e) the module length is plotted for each 2D irradiance map.

3. SIMULATION RESULTS

3.1 Torque-tube-reflected irradiance on a summer and winter day

The torque tube reflection incident on the rear of the module varies over the course of a day and year for both 1P and 2P systems. To illustrate, we show the torque-tube-reflected irradiance on a summer sunny day (June 19), and winter sunny day (December 22) for 1P (Figure 3) and 2P (Figure 4) configurations with 0.2 albedo. The timestamps shown are two hours after sunrise (black, solid line), noon (grey, dashed line), and two hours before sunset (red, dotted line). The morning and evening timestamps shown do not require backtracking.

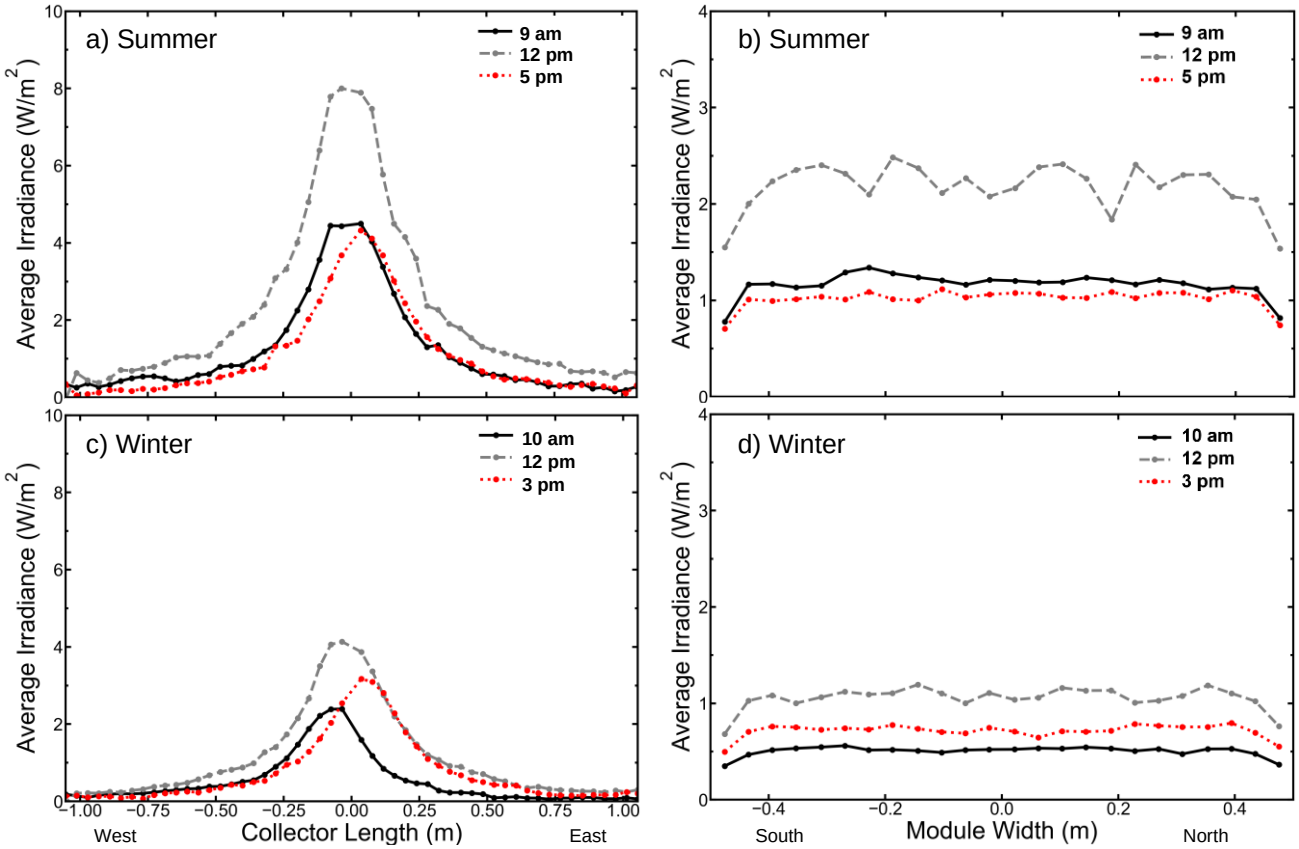

Figure 3. Average torque-tube-reflected irradiance taken along the module width (left), and along the collector length (right), for the 1P configuration with 0.2 albedo, on a summer sunny day (top) and winter sunny day (bottom).

On both the summer (Figure 3a and b) and winter (Figure 3c and d) days, the 1P torque tube reflection is highest in the middle of the day. The irradiance peak is on the western half of the module in the morning and shifts towards the eastern half of the module in the evening as it tracks the sun (Figure 3a and c). The fraction of diffuse and ground-reflected light hitting the torque tube determines which side of the module receives more torque-tube-reflected irradiance. Diffuse light reflects off the torque tube and primarily onto the side of the module higher in the sky (west in the morning; east in the evening), while ground-reflected light incident on the torque tube reflects more strongly onto the side of the module closer to the ground (east in the morning; west in the evening). Therefore, changing albedo or weather, which can affect the amount of ground-reflected or diffuse light incident on the torque tube, can alter the location of the torque-tube-reflected irradiance peak from east to west along the module. For instance, on the winter day with 0.6 albedo (not shown in Figure

3) and the winter day with 0.2 albedo, the torque-tube-reflected irradiance peak follows the same path across the module throughout both days. However, on the summer day with 0.6 albedo (not shown in Figure 3), the torque-tube-reflected irradiance peak locations are reversed compared to the 0.2 albedo case. This is caused by the higher diffuse irradiance in the winter and the higher ground-reflected irradiance in the summer for this site configuration.

The shift in the peak torque-tube-reflected irradiance from east to west over the course of the day is less significant in the 2P modules with 0.2 albedo (Figure 4a and c). Direct light incident on the front of the torque tube (via the TT gap) increases the 2P torque-tube-reflected irradiance up to nearly 6-times that of the 1P configuration (note the difference in irradiance scales between Figure 3 and Figure 4) and reflects evenly onto the east and west modules during non-backtracking hours. Thus, the shift in peak torque-tube-reflected irradiance from East to West over the day, due to the diffuse and ground-reflected light contributions, is small compared to the total torque-tube-reflected irradiance.

The direct light incident on the torque tube in 2P configurations also impacts the shape of the torque tube reflection signal along the North-South direction (Figure 4b and Figure 4d). The decreased torque-tube-reflected irradiance on the southern side of Figure 4d can be attributed to the module supports shading the southern edge of the module from direct light reflected off the torque tube. During winter in the Northern hemisphere, the sun's low elevation leads the module supports to cast longer shadows on the Southern portion of the torque tube than they do in the summer.

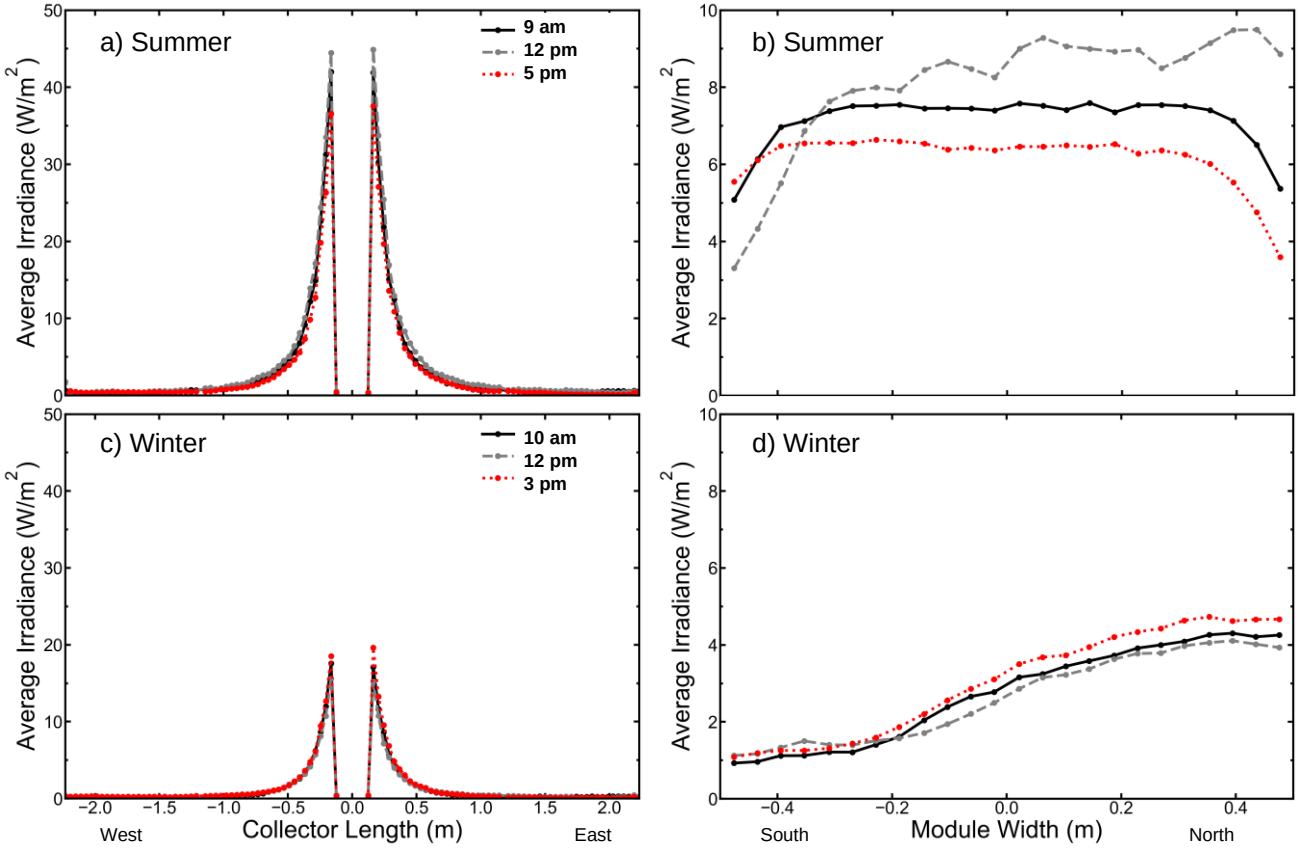

Figure 4.Torque tube reflection for a summer sunny day (top) and winter sunny day (bottom) on a pair of 2P modules with 0.2 albedo. Average torque-tube-reflected irradiance taken along the module width (left), and along the module length (right).

3.2 Hourly impact of torque tube reflection

We investigated each hour of the day separately by calculating an hour-wise annual average torque-tube-reflected irradiance map for each non-zero irradiance timestamp for both 1P (Figure 5a) and 2P (Figure 5b) systems. In the 2P case,

the torque tube is not shaded by the modules and direct irradiance that passes through the torque tube gap illuminates the torque tube and can be reflected to the rear of the module, resulting in higher torque-tube-reflected irradiance. In the 1P case, by comparison, most light incident on the torque tube is ground-reflected and diffuse light, resulting in lower total torque-tube-reflected irradiance. These effects are illustrated by the difference in irradiance scales for each configuration (comparing Figure 5a and b), with 2P peak torque-tube-reflected irradiance reaching nearly 6-times that of 1P. Midday hours, when global irradiance is highest, demonstrate the most torque-tube-reflected light for both 1P and 2P systems. The frame sections perpendicular to the torque tube block torque-tube-reflected irradiance on the North and South edges of the module near the torque tube, and, in the 2P system, the frame adjacent and parallel to the torque tube shades the torque-tube-reflected irradiance. Frameless modules can therefore benefit more from torque tube reflection.

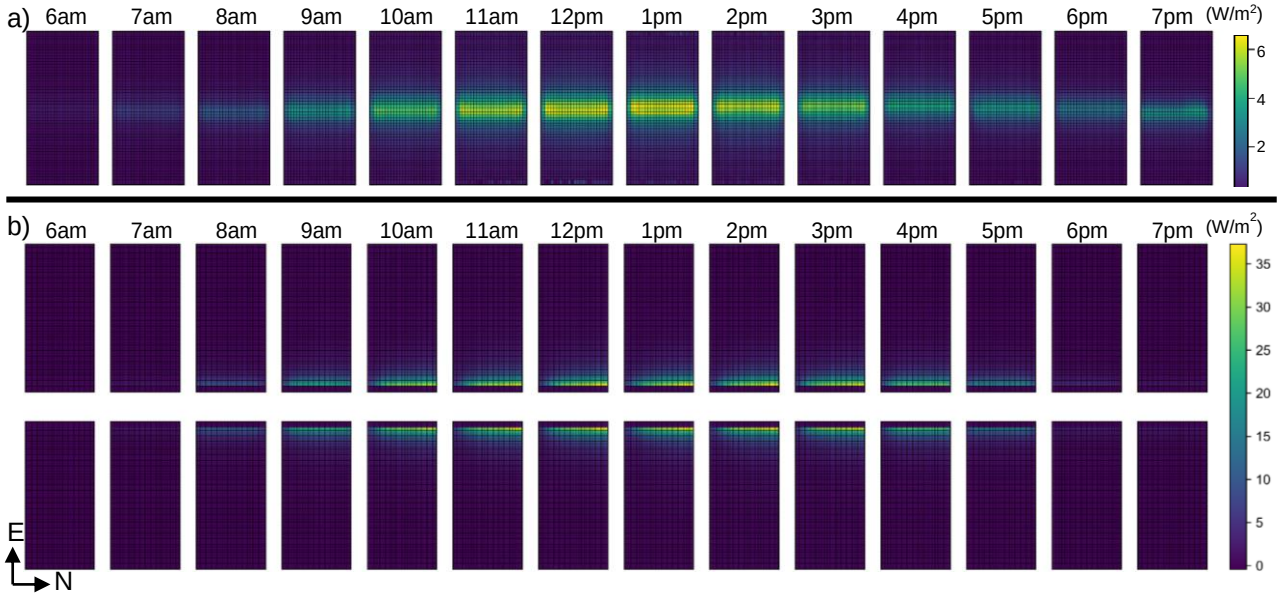

Figure 5. Average annual torque-tube-reflected irradiance maps for each non-zero irradiance hour in the day. (a) 1P and (b) 2P configurations. Note the difference in scales between (a) and (b).

3.3 Torque tube insolation fraction

The fraction of rear-side insolation contributed by torque tube reflection is given by

$$\text{Torque Tube Insolation Fraction [\%]} = \frac{\sum_{t=1}^{T} \bar{G}_{\text{TT}_t}}{\sum_{t=1}^{T} \bar{G}_t} \quad (1)$$

where $\bar{G}_{\text{TT}_t}$ is the average module rear-side insolation due to torque tube reflection (Wh/m^2) and $\bar{G}_t$ is the average module rear-side insolation (Wh/m^2), for timestamp t out of T total timestamps. The average module rear side insolation is taken from the reflecting torque tube case, not the absorptive torque tube case.

For the 1P case, in Figure 6a, the proportion of rear-side irradiance contributed by torque tube reflection is flat at about 3% over the course of a day. Overall, despite minimal direct irradiance on the torque tube, the 1P module has a similar relative contribution of torque tube reflection to rear insolation as the 2P case at 0.6 albedo.

For the 2P case, in Figure 6b, the proportion of rear insolation from torque tube reflection is highest for the 0.2 albedo case due to reduced total rear-side irradiance. Direct light that passes through the torque tube gap onto the torque tube, and is reflected to the rear face remains constant with albedo. Thus, for smaller albedo, where there is less ground-reflected

irradiance and therefore less total rear irradiance, the torque tube reflection contributes a larger portion of the total rear irradiance.

Similarly, the fraction of rear-side irradiance contributed by the torque tube reflection is highest in mid-morning and mid-afternoon for both albedos. In the first few hours of the day, the torque tube irradiance increases faster than the total rear-side irradiance. After mid-morning (around 9-10am), the torque-tube-reflected irradiance plateaus but the total rear-side irradiance continues to increase into midday. Therefore, despite the torque-tube-reflected irradiance being highest at solar noon, the fraction of rear irradiance contributed by the torque tube reflection exhibits a valley in the middle of the day and peaks in the late morning and evening hours; varying over this middle section of the day from 4.6%-7.2% and from 2.5%-4.4% for 0.2 albedo and 0.6 albedo, respectively, as shown in Figure 6b.

There is a higher fraction of total rear irradiance contributed by torque tube reflection on the eastern module in the morning, and on the western module in the evening for both albedos (Figure 6b). This is due to reduced total rear irradiance on the eastern module in the morning and on the western module in the evening. As the module nearer to the ground, these modules receive less diffuse irradiance and therefore have smaller total rear irradiance. A smaller total rear irradiance results in a larger relative contribution from torque tube reflection.

Altogether, for an albedo of 0.6, torque tube reflection accounts for 2.9% and 3.1% of the annual rear insolation in 1P and 2P configurations, respectively. When the albedo is 0.2, torque tube reflection accounts for 3.0% and 5.5% of the annual rear insolation in 1P and 2P configurations, respectively. The relative contribution to 2P module rear insolation from torque tube reflection is higher for 0.2 albedo than for 0.6 albedo because there is a higher fraction of direct light in this case. A similar shift is not observed in the 1P case because no direct light hits the torque tube in the 1P configuration.

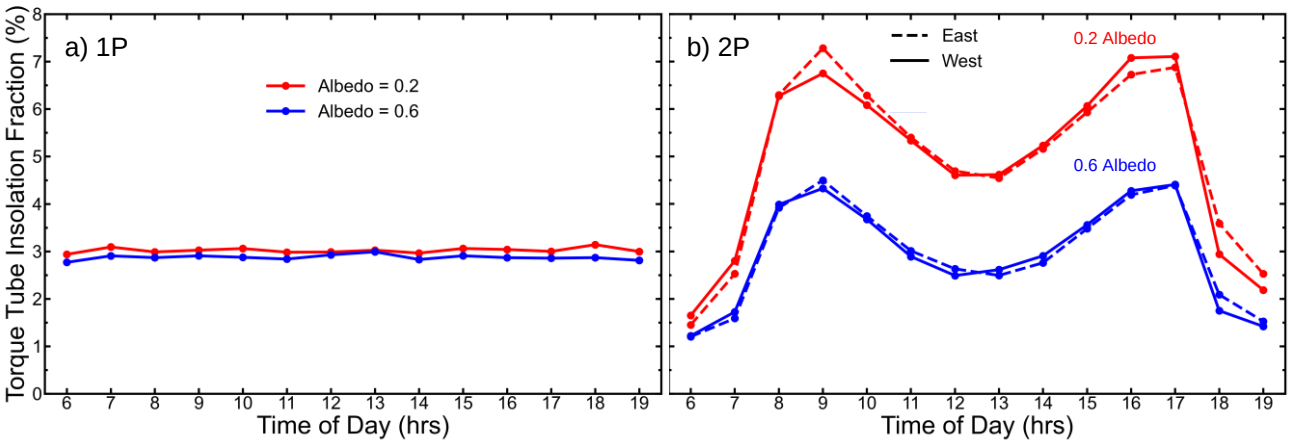

Figure 6. Average annual hourly fraction of total rear insolation due to torque tube reflection for (a) 1P and (b) 2P.

3.4 Hourly insolation mismatch

In addition to the total insolation added to the rear of the module by the torque tube reflection, the irradiance *distribution* across the module can also critically impact its performance. Irradiance mismatch is a measure of the spatial non-uniformity of the incident irradiance across a module at a given time. For a given timestamp *t*, the irradiance mismatch can be quantified by the mean absolute difference (MD) of irradiance across all irradiance calculation points.

$$MD_t\ [\mathrm{W/m^2}] = \frac{1}{n^2}\sum_{i=1}^{n}\sum_{j=1}^{n}\left|G_i - G_j\right| \tag{2}$$

where n is the number of total sample points on the modules, and G_i and G_j are the irradiance (W/m^2) at point i and point j, respectively [19]. We are investigating rear-side irradiance, but a similar approach can be taken for the front side. This instantaneous irradiance mismatch can vary widely over time, and translates to an instantaneous electrical loss in a non-linear relationship, as described in [20].

The relative mean absolute difference (RMD) in insolation provides a metric to compare irradiance mismatch between systems over T total timestamps and is given by:

$$RMD\ [\%] = \frac{\sum_{t=1}^{T} MD_t * \tau}{\sum_{t=1}^{T} \bar{G}_t} \tag{3}$$

where MD_t is the mean absolute difference between irradiance samples (W/m^2), τ is the timestamp duration (h), and, as above in Equation (1), $\bar{G}_t$ is the average module insolation (Wh/m^2), for timestamp t. This value is not directly equivalent to the total electrical mismatch loss over T total timestamps, and differs from the instantaneous irradiance of any one timestamp. Instead, it provides a measure of the irradiance spatial variation over one or multiple timestamps relative to the total insolation. RMD will be referred to as the rear insolation mismatch below.

Figure 7a shows the hour-wise annual average rear insolation mismatch of the 1P module under test with a reflective (triangles) and an absorptive (circles) torque tube, for 0.2 (red) and 0.6 (blue) albedo, by time of day. For both albedos, rear insolation mismatch is lower with the reflective torque tube than the absorptive torque tube, meaning that the torque tube reflection partially offsets the effect of torque tube shading in 1P modules. The difference in insolation mismatch (Figure 7b) is the impact of the torque tube reflection. Incorporating torque tube reflection decreases rear insolation mismatch by roughly 1% for both 0.2 and 0.6 albedo at every hour the day for the 1P case.

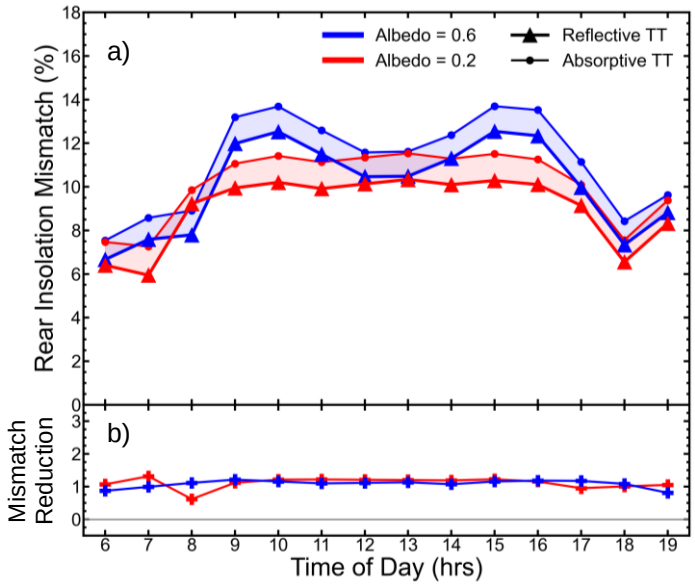

Figure 7. Rear insolation mismatch for the center module in a 1P array, as calculated in Equation (3), averaged over the year for each time of day. Both the reflective torque tube and absorptive torque tube cases are shown in (a); the difference (b) shows the effect of the torque tube reflection signal on rear insolation mismatch.

For the 0.2 albedo case, annual rear insolation mismatch is highest in the middle of the day. The mismatch does not dip down in the midday hours, as opposed to the 0.6 albedo case where the insolation mismatch peaks in the mid-morning and mid-afternoon (Figure 7a). The peaks in rear insolation mismatch for the 0.6 albedo case are due to one half of the module being tilted closer to the ground at these times, combined with the increased ground-reflected light at higher albedo, resulting in larger rear irradiance non-uniformities across the module length. Conversely, in the middle of the day when the module is near parallel to the ground, rear insolation mismatch is almost identical for 0.2 and 0.6 albedo.

Similar to the 1P module, torque tube reflection decreases annual rear insolation mismatch for 2P modules in both the 0.2 and 0.6 albedo cases (Figure 8a and Figure 8b, respectively). Insolation mismatch is higher for the eastern module (dashed lines) in the morning and the western module (solid lines) in the evening (i.e. the module closer to the ground). As shown in Figure 8c and Figure 8d, the difference in total insolation mismatch on the 2P modules between the absorbing and reflecting torque tube cases varies throughout the day. This difference in insolation mismatch can even be negative for the 0.2 albedo case on the module tilted higher in the sky, indicating torque tube reflection increases the rear insolation mismatch up to 0.6%. Although, at most times, the difference in insolation mismatch is positive and larger than in the 1P scenario; up to 2.9% and 2.0% for the 0.2 albedo and 0.6 albedo cases, respectively.

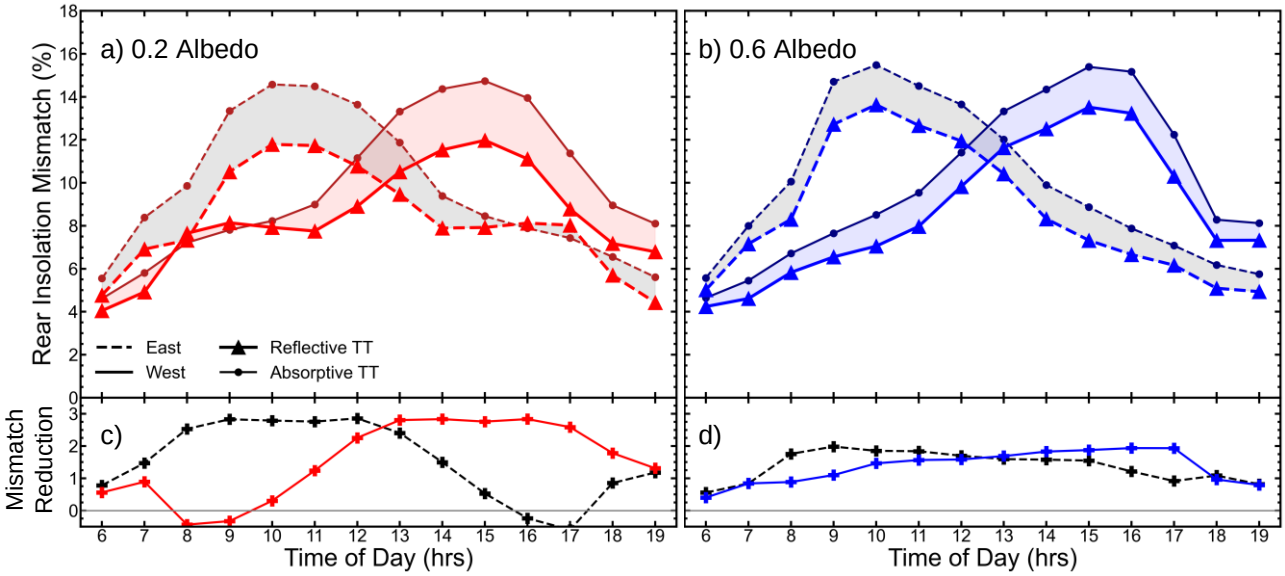

Figure 8. Rear insolation mismatch for the center module in a 2P array averaged over the year for each hour, for (a) 0.2 albedo, and (b) 0.6 albedo. Both the reflective torque tube and absorptive torque tube cases are shown; the difference is plotted in (c) and (d), demonstrating the impact of the torque tube reflection on rear insolation mismatch. Red: 0.2 albedo; blue: 0.6 albedo; dashed: eastern module; solid: western module.

3.5 Monthly fraction of rear insolation from torque tube reflection

Just as torque-tube-reflected insolation varies over the course of the day, it also varies over the course of the year. In Figure 9, the monthly torque tube insolation fraction is given for each month of the year for (a) the 1P system and (b) the 2P system, as calculated in Equation (1). For both the 1P and 2P systems, the 0.2 albedo case has a higher torque-tube-reflected insolation fraction than the 0.6 albedo case. This is due to lower total rear irradiance in the 0.2 albedo case, resulting in a larger torque-tube-reflected fraction of rear irradiance. In the 1P system, torque-tube-reflected light is primarily caused by diffuse and ground-reflected irradiance, and the fraction of rear insolation from torque tube reflection is relatively constant at around 3% for each month in the year. For the 2P system, where a large portion of torque-tube-reflected irradiance is caused by direct light, torque tube reflections contribute a higher fraction of total rear irradiance in the summer when direct irradiance is highest.

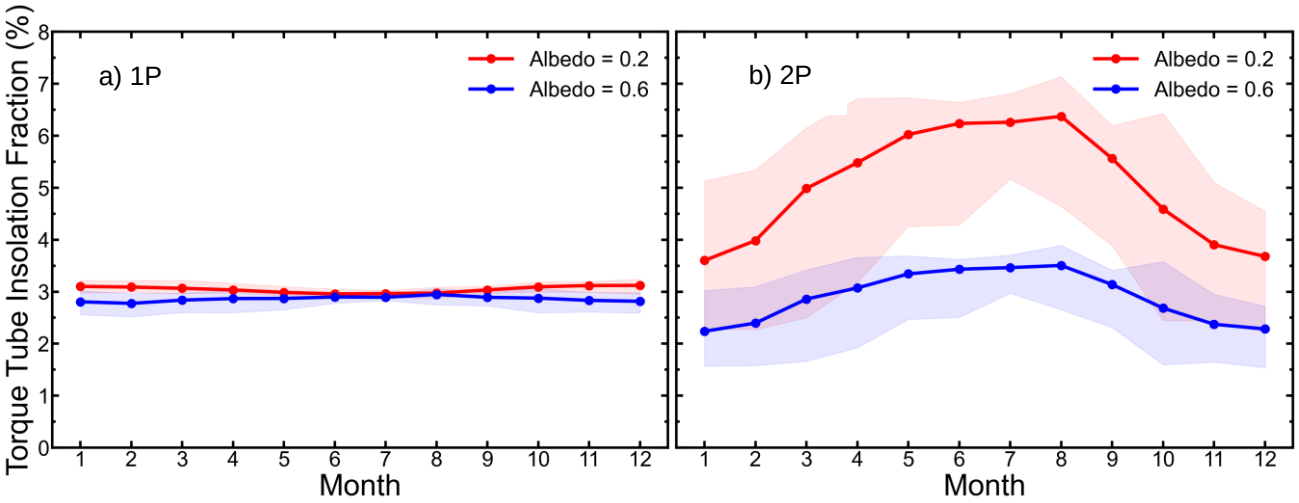

Figure 9. Monthly torque tube reflection insolation as a percentage of total rear insolation with a reflective torque tube for (a) 1P and (b) 2P modules. Curves indicate the average torque tube insolation fraction of all days for each month, and the colored bounds indicate the total range (minimum and maximum value) of daily torque-tube-reflected insolation fraction for each month.

Given the fraction of rear insolation from torque-tube-reflected light remains relatively constant in the 1P system for each month in the year (Figure 9a) and for each hour in the day (Figure 6a), bifacial energy yield models may be able to account for torque tube reflection in 1P systems as a constant factor. Conversely, the torque tube shadow affects 1P rear insolation mismatch on an hourly basis (Figure 7a), as shown by both the absorptive torque tube (circles) and the reflective torque tube (triangles). Thus, a detailed torque tube shading model must be considered to accurately predict rear-side insolation in 1P systems. However, the torque tube reflection reduces the rear insolation mismatch by an approximately constant value of 1% each hour of the day (Figure 7b), suggesting that a detailed shading model paired with a constant illumination factor may be sufficient to accurately calculate 1P bifacial yield. The same cannot be said for 2P systems because the fraction of rear insolation from torque-tube-reflected irradiance varies for each month in the year (Figure 9b) and for each hour in the day (Figure 6b).

4. CONCLUSIONS

In this work, we modelled the impact of incorporating a reflective torque tube on rear insolation and rear insolation mismatch for 1P and 2P SAT systems at the BiTEC site in Livermore, California. We demonstrated that torque-tube-reflected irradiance is focused near the torque tube, where torque tube shading is strongest. Torque tube reflection was shown to partially offset the effects of torque tube shading by increasing rear irradiance and decreasing rear-side irradiance mismatch in both 1P and 2P systems, and for both 0.2 and 0.6 albedos.

For the 1P system, torque tube reflection increased annual rear-side insolation by 3.0% and 2.9% for 0.2 albedo and 0.6 albedo, respectively, and reduced annual rear side insolation mismatch by 1.1% for both albedos. The torque-tube-reflected rear insolation fraction remained at 3% throughout the day, implying that the increase in rear irradiance due to torque tube reflection in 1P systems may be accounted for with a single correction factor. However, the hourly rear insolation mismatch varied hour by hour throughout the day from 5.9-10.3% and from 6.7-12.5% for 0.2 albedo and 0.6 albedo, respectively, due to torque tube shading. Therefore, for accurate 1P system bifacial energy yield prediction, torque tube shading should be accounted for on at least an hourly basis.

For a comparable 2P system, torque tube reflection increased annual rear insolation by 5.5% and 3.1% for 0.2 albedo and 0.6 albedo, respectively. In contrast to the 1P system, the 2P system's fraction of rear insolation from torque tube reflection rear insolation varied hour by hour throughout the day from 1.5-7.2% and from 1.2-4.5% for 0.2 albedo and 0.6 albedo, respectively, implying that torque tube reflection should be accounted for on at least an hourly basis instead of with a single correction factor. In addition, the 2P system's rear insolation mismatch varied hour by hour throughout the day from

4.1-12.0% for 0.2 albedo and from 4.2-13.6% for 0.6 albedo, indicating that torque tube shading should be accounted for on at least an hourly basis in the 2P system for accurate bifacial yield prediction, as in the 1P system. Incorporating torque tube reflection in the 2P system reduced the annual rear insolation mismatch by 1.5% and 1.7% for 0.2 albedo and 0.6 albedo, respectively, with some variation based on time of day, further suggesting 2P systems require torque tube reflection to be accounted for on at least an hourly basis.

We demonstrated that bifacial PV models that account for the effects of varying torque tube shading and reflections on an hourly basis can better represent real-world systems over the course of a day and year for both 1P and 2P systems. Unlike 2P systems, torque tube reflection in 1P systems may be simplified by applying a constant factor to the total rear irradiance.

REFERENCES

[1] "International Technology Roadmap for Photovoltaic (ITRPV) 2020 Results," in International Technology Roadmap for Photovoltaic" 12th edition, March 2021, <https://itrpv.vdma.org/documents/27094228/29066965/20210ITRPV/08ccda3a-585e-6a58-6afa-6c20e436cf41> (March 2021)

[2] M. Koussa, A. Cheknane, S. Hadji, M. Haddadi, and S. Noureddine, "Measured and modelled improvement in solar energy yield from flat plate photovoltaic systems utilizing different tracking systems and under a range of environmental conditions," Appl. Energy, 88(5), 1756–1771 (2011).

[3] C. D. Rodríguez-Gallegos et al., "Global Techno-Economic Performance of Bifacial and Tracking Photovoltaic Systems," Joule, 4(7), 1514–1541 (2020).

[4] R. Kopecek and J. Libal, "Towards large-scale deployment of bifacial photovoltaics," Nature Energy, 3, 443-446 (2018).

[5] J. Guerrero Pérez, I. Muñoz Benavente, and J. Navarro Berbel, "BiTEC Results 4 - Fall 2018 - Fall 2019: The Bifacial Year," Soltec, 2019, [Online]. Available: <https://lab.soltec.com/bifacial-trackers-ii/> (2019).

[6] J. S. Stein et al., "Bifacial Photovoltaic Modules and Systems: Experience and Results from International Research and Pilot Applications," Report IEA-PVPS T13-14 (2021).

[7] K. R. McIntosh, M. D. Abbott, B. A. Sudbury, and J. Meydbray, "Mismatch Loss in Bifacial Modules Due to Nonuniform Illumination in 1-D Tracking Systems," IEEE J. Photovoltaics, 9(6), 1504–1512, (2019).

[8] A. C. J. Russell, C. E. Valdivia, M. R. Lewis, J. E. Haysom, and K. Hinzer, "Modelling energy yield including rack shading for single-axis tracked bifacial solar panels," in 2019 Photonics North, 58891, (2019).

[9] S. A. Pelaez, C. Deline, J. S. Stein, B. Marion, K. Anderson, and M. Muller, "Effect of torque-tube parameters on rear-irradiance and rear-shading loss for bifacial PV performance on single-axis tracking systems," in 46th IEEE PVSC, vol. 2, pp. 3525–3530, (2019).

[10] S. Ayala Pelaez and C. Deline, "Bifacial_Radiance: a Python Package for Modeling Bifacial Solar Photovoltaic Systems," J. Open Source Softw., 5(50), 1865, (2020).

[11] S. A. Pelaez, C. Deline, S. M. Macalpine, B. Marion, J. S. Stein, and R. K. Kostuk, "Comparison of Bifacial Solar Irradiance Model Predictions with Field Validation," IEEE J. Photovoltaics, 9(1), 82–88, (2019).

[12] S. A. Pelaez, C. Deline, P. Greenberg, J. S. Stein, and R. K. Kostuk, "Model and Validation of Single-Axis Tracking with Bifacial PV," IEEE J. Photovoltaics, 9(3), 715–721, (2019).

[13] C. Deline, S. Macalpine, B. Marion, F. Toor, A. Asgharzadeh, and J. S. Stein, "Assessment of Bifacial Photovoltaic Module Power Rating Methodologies-Inside and Out," IEEE J. Photovoltaics, vol. 7, no. 2, pp. 575–580, (2017).

[14] G. W. Larson and R. A. Shakespeare, [Rendering with Radiance: The Art and Science of Lighting Visualization]. Morgan Kaufmann Publishers (1998).

[15] S. Crone, [Radiance Users Manual], vol. 2, (1992).

[16] J. Guerrero Pérez and J. Navarro Berbel, "BiTEC : How to simulate bifacial projects?," Madrid, Spain, 2019, <https://lab.soltec.com/bifacial-trackers-ii/> (2019).

[17] T. Ribbon and T. R. Technology, "Tiger Bifacial DG Higher lifetime Power Yield," 2015, <https://jinkosolar.eu/files/jinko/download/2020/datasheet/TR JKM445-465M-7RL3-BDVP-D4-EN.pdf> (2015).

[18] W. F. Holmgren, R. W. Andrews, A. T. Lorenzo, and J. S. Stein, "PVLIB Python 2015," in 42nd IEEE PVSC, 1–5, (2015).

[19] C. Deline, S. Ayala Pelaez, S. MacAlpine, and C. Olalla, "Bifacial PV mismatch loss estimation and parameterization," in 36th EU PVSEC, no. 1, 1–5, (2019).

[20] C. Deline, S. Ayala Pelaez, S. MacAlpine, and C. Olalla, "Estimating and parameterizing mismatch power loss in bifacial photovoltaic systems," Prog. Photovoltaics Res. Appl., 28(7), 691–703, (2020).

Chapter 4: Torque Tube Reflection Electrical Performance

4.1 Preface and Author Contributions

This chapter contains a manuscript in print with Optics Express. The manuscript builds on the work from Chapter 3 by quantifying the impact of TT reflection on energy yield and electrical mismatch, and quantifying the impact of an incidence angle modifier on TT reflection. In addition, the TT reflection analysis is based on sun zenith and DHI fraction instead of time of day to better represent more consistent illumination conditions across the year. The article concludes that TT reflection reduces electrical mismatch by partially offsetting TT shading, and increases annual energy yield by 0.17% and 0.30% in our particular 1P and 2P systems. While the overall impact of TT reflection is greater in the 2P system, the TT reflection's greatest instantaneous relative contribution to total energy yield is larger for the 1P system, at high DHI fractions and sun zeniths. Simulations, analysis, and lead writing performed by T. J. Coathup. Contributions from authors: M. R. Lewis, advice, writing, and edits; A. C. J. Russell, simulation, advice, and writing; Joan E. Haysom, conceptualization; C. E. Valdivia, advice, and writing; K. Hinzer, conceptualization and writing.

4.2 Publication - Accepted January 2023

Trevor J. Coathup, Mandy R. Lewis, Annie C. J. Russell, Joan E. Haysom, Christopher E. Valdivia, Karin Hinzer, "Impact of Torque Tube Reflection on Bifacial Photovoltaic Single Axis Tracked System Performance," in print Optics Express January 2023.

Impact of Torque Tube Reflection on Bifacial Photovoltaic Single Axis Tracked System Performance

TREVOR J. COATHUP,[1] MANDY R. LEWIS,[1] ANNIE C. J. RUSSELL[1], JOAN E. HAYSOM,[1,2] CHRISTOPHER E. VALDIVIA[1], AND KARIN HINZER[1]

[1]*SUNLAB, School of Electrical Engineering and Computer Science, University of Ottawa, Ottawa, Ontario, K1N 6N5, Canada*
[2]*J. L. Richards and Associates Ltd., Ottawa, Ontario, K1S 1N4, Canada*

Abstract: Among the racking elements of bifacial photovoltaic (PV) single-axis tracked systems, the torque tube (TT) introduces the most shading and reflection, increasing irradiance nonuniformity and electrical mismatch loss. We simulate the impact of TT shading and reflection on the irradiance profiles, electrical mismatch, and energy yield for central bifacial PV modules on one-in-portrait (1P) and two-in-portrait (2P) single-axis trackers. TT reflection increases annual irradiance in 1P and 2P systems by 0.17% and 0.30%, respectively. Overall, TT reflection increases the predicted instantaneous energy yield by up to 0.8% and 0.4%, and the annual energy yield by 0.11% and 0.18% in 1P and 2P system, respectively.

1. Introduction

Bifacial photovoltaic (PV) modules have greater energy yield than traditional monofacial modules due to their ability to convert both front and rear irradiance to electrical energy. Single-axis tracking systems can further increase yield and reduce the levelized cost of energy [1] by rotating the modules throughout the day to maximize the illuminated cross-sectional area, reducing cosine and angle of incidence (AOI) losses [2]. PV modules are subject to power loss caused by electrical mismatch from varying cell maximum power points due to manufacturing tolerances, temperature gradients, and irradiance nonuniformity stemming from many factors including object shading, passing clouds, soiling, and proximity to the ground [3–6]. Racking elements in single-axis tracking systems introduce both shade and reflections on the rear face, increasing rear irradiance nonuniformity and causing electrical mismatch that reduces module power [7]. These effects lead to decreased bifacial energy yield gain and can create damaging hot spots in extreme cases [8]. The effects of racking, particularly from the torque tube (TT) as it spans the middle of the rear collector surface, must be accurately quantified in energy yield predictions to further reduce investor risk, increase stakeholder confidence, and hasten the adoption of tracked bifacial PV [9].

Existing field-validated ray tracing bifacial PV modeling software like bifacial_radiance [10–12] and others [13–17] can capture both shading and reflections from racking elements at a high computational cost by simulating many stochastic rays interacting with multiple textured surfaces. On the other hand, two-dimensional (2D) [18–26] and three-dimensional (3D) view factor models [27–31] estimate racking shading with user-defined loss factors, known as shading factors, which can be set as annual average values calculated by comparing PV performance with and without racking [22-25], or account for racking shading using simulations of instantaneous ray-object intersection [26]. Finally, hybrid modeling approaches employ a view factor method for the front irradiance while capturing the impacts of racking with ray tracing for the rear irradiance only [32]. Comparisons of PV modeling software have been shown previously in Refs. [33, 34]. One possible enhancement of 3D view factor models with

detailed shading accounted for using ray-object intersection is the inclusion of reflections from racking elements, specifically the TT. However, the isolated impact of racking reflections on PV performance is not well documented.

McIntosh *et al.* showed that the relative reduction in module power due to nonuniform illumination, including racking shading, is greatest at solar noon in sunny conditions, and greater for one-in-portrait (1P) than two-in-portrait (2P) single-axis tracker frameless modules, decreasing central module yield by 0.23% and 0.09% respectively [7]. However, the racking reflection's contribution was not isolated. Deline *et al.* found annual mismatch losses of less than 0.5% for 1P single-axis tracked systems [4]. Guerrero Pérez *et al.* showed, for a sunny summer day, the rear insolation in a 2P single-axis tracker decreased by 12% with an absorptive TT but only 1.3% with a reflective TT [35]. Our previous work extended this to compare the impact of TT reflection in both 1P and 2P trackers. We showed that including a reflective TT surface rather than a fully absorptive surface increased annual rear insolation by 3% and 5.5% for modules on 1P and 2P single-axis trackers, respectively [36]. However, the impact of racking reflection on *energy yield* was not reported.

In this work, we quantify the impact of TT reflection on irradiance, electrical mismatch, and total energy yield based on sun position and sky condition using a hybrid modeling approach with a ray tracing model, bifacial_radiance [10–12] to extract the TT reflection. We introduce this reflection as an additional irradiance source in DUET [31], a 3D view factor model with detailed shading, to assess the impact of TT reflection in such a model. Using DUET, we can also include and quantify the impact of an incidence angle modifier (IAM) on the TT reflection's contribution to energy yield. Isolating the TT reflection and accounting for angle of incidence losses was not possible with either simulation method alone, thus bifacial_radiance and DUET are appropriate for this work. First, we will describe the model and the system configuration of the modeled PV arrays. Next, we will discuss the integration of TT-reflected light from bifacial_radiance into DUET. Finally, we will present the impact of TT reflection.

2. Simulation method

2.1 Site Description

We modeled a 2P array after the Bifacial Tracker Evaluation Center (BiTEC) site in Livermore, California, USA (37.70° N, 121.82° W, 121 m elevation), and a comparable 1P array [35]. The 1P (and 2P) array included 5 rows of 23 (pairs of) modules in horizontal single-axis tracking configuration with north-south alignment of the TT, and a ground cover ratio of 0.456 (Fig. 1a and b). The modeled ground albedo is 0.2, emulating the flat terrain at the BiTEC site [35], and

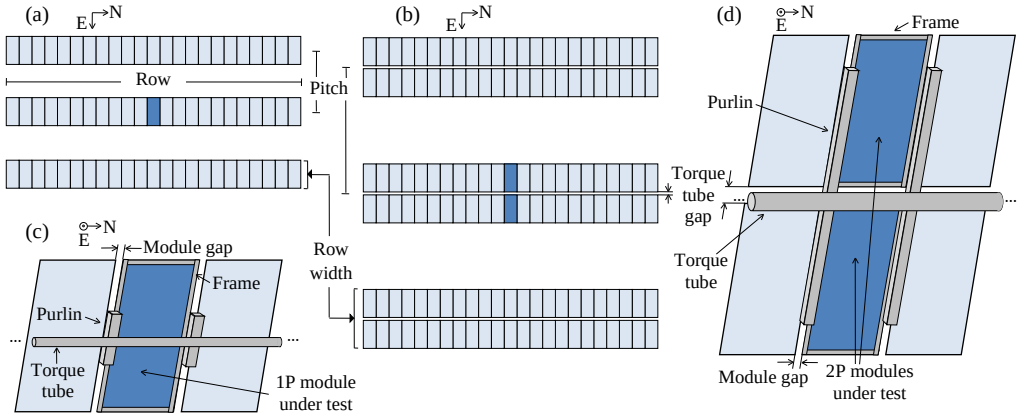

Fig. 1. Center 3 of 5 rows in the (a) 1P and (b) 2P arrays with the collector under test highlighted in dark blue. Frame and purlins modeled on the (c) 1P and (d) 2P rear side of collector under test with the TT spanning the row under test. Portrait configuration means the modules' long sides are oriented perpendicular to the torque tube.

is assumed to be spectrally flat. Locations with higher albedo will show increased energy yield [37].

Modeling parameters (see Appendix A) emulate a Soltec SF7 2P tracker and a comparable 1P configuration, each with a round TT. The TT diameter is 0.1 m and 0.21 m in the 1P and 2P system, respectively, making the ratio of the TT diameter to the row width identical when including the 0.15 m gap between the east and west modules in the 2P system. The collector tilt angle follows sun position and is calculated by pvlib's tracking algorithm [38], with a maximum tracking angle of ±60° and backtracking enabled to avoid row-to-row shading.

The module's geometrical and electrical properties emulate the 460 W Jinko Solar Tiger Bifacial JKM460M-7R13-TV module [39], which includes two parallel strings of 13×2 half-cut cells connected to each of its three bypass diodes. The module frame spans the module edges, with side lengths of 1.032 m and 2.205 m, a thickness of 0.03 m perpendicular to the module face, and an overhang of 0.01 m below the rear of the module.

Purlins connect the module frame and the TT, running perpendicular to the TT. The purlins are 0.08 m tall between the TT and the frame, 0.03 m wide, bridging the gap between modules along the row, and 0.44 m and 2.8 m long for the 1P and 2P configurations, respectively. Frames and purlins were included in the model only for the *collector under test* (Fig. 1c and d) which is the module in the center of the array in the 1P system, and the east and west module pair in the center of the array in the 2P system. Unless otherwise stated, the collector values reported for the 2P system are taken as an average of the east and west central module values. The TT was modeled on the center row, spanning the length of the entire row. Piles were not included in the array geometry to allow these single-collector results to be interpreted more generally. The reflectivity of all racking components (frame, purlins, TT) was set to 0.745, with a specularity of 0.9 and roughness of 0.2, emulating the racking materials at the BiTEC site [35].

2.2 Software Description & Implementation

Using hourly typical meteorological year (TMY) data from the United States (US) National Solar Radiation Database (NSRDB) [40], we calculated the irradiance and electrical performance for the central collector of both the 1P and 2P systems. First, the systems were modeled with bifacial_radiance [10–12] (version 0.3.4), an open-source software by the US National Renewable Energy Laboratory (NREL), built around the open-source ray tracing software RADIANCE [41]. To isolate the impact of racking reflections, frames and purlins were added to the collector under test in bifacial_radiance and were rotated with the tracker as it tracked the sun throughout the day. In this work, the irradiance of the collector under test was sampled in a 2D array of 52×24 sample points, i, per module face. This sampling resolution on the 26×6 half-cut cell module allows for 2×4 equally spaced sample points per cell. This high resolution captures the nonuniform irradiance profile near the module edges and racking elements.

We used bifacial_radiance to isolate the TT-reflected light incident on the collector under test, henceforth referred to as the *TT reflection*. The PV systems were simulated twice using bifacial_radiance: once with a fully absorptive TT surface (reflectivity of 0); and again with the reflective TT surface. The frame and purlins were reflective for all cases simulated in bifacial_radiance. The TT reflection, G_{TT}, was calculated for each sample point, i, and for each timestamp, t, using

$$G_{\mathrm{TT}_{i,t}} = G_{\mathrm{TTA}_{i,t}} - G_{\mathrm{TTR}_{i,t}} \quad (1)$$

where G_{TTA} is the rear irradiance with the absorptive TT and G_{TTR} is the rear irradiance with the reflective TT.

Next, we modeled the PV systems with DUET, our 3D view factor model with detailed shading and an integrated electrical model created by the SUNLAB at the University of Ottawa [31]. In DUET, we simulated the PV array with and without the TT reflection imported from

bifacial_radiance to quantify its impact on irradiance, electrical mismatch, and overall energy yield. The sun position and collector tilt angle were set in DUET to be identical to the bifacial_radiance values, as determined by pvlib, at each timestamp. The baseline DUET case includes a fully absorptive TT, absorptive frames, and absorptive purlins. The TT reflection, as calculated in bifacial_radiance, is added to the baseline DUET case for the reflective TT scenario, and nothing is added to the baseline DUET case for the absorptive TT scenario.

Since the TT is not modeled as a reflecting surface in DUET, the TT reflection, as calculated in bifacial_radiance, is added to each sample point on the collector as an additional irradiance source. Due to the TT's proximity to the collector, the TT reflection typically has a high AOI. Glass, encapsulant, and Si layers of the module were not modeled in bifacial_radiance, so the computed irradiance represents only the total irradiance incident at each sample point on the module surface. To estimate the AOI, we assumed reflections to be uniformly distributed across the TT. An average IAM for each collector sample point was then determined for the array geometry, accounting for frame shading. This 2D effective irradiance profile from the TT reflection was then added to the IAM-corrected rear illumination profiles for sky and ground-reflected light within the electrical calculations in DUET (Appendix B).

3. Results and discussion

Of all racking elements, the TT provides the greatest change in total irradiance and irradiance profile due to reflections [42], with the greatest impact near the TT. In the 2P system, front-incident direct and diffuse light can pass through the TT gap to reflect off the TT and onto the rear face of the collector, increasing rear side irradiance. Conversely, in 1P systems, direct irradiance incident on the TT is relatively low, and the TT shades a larger portion of the collector rear surface, leading to increased electrical mismatch losses. We will show that TT reflection offsets TT shading, increases irradiance, and decreases electrical mismatch in most cases, resulting in increased total energy yield.

3.1 Irradiance

Global horizontal irradiance (GHI) is the sum total of all light incident on a horizontal surface and is comprised of direct normal irradiance (DNI), incident at a single angle on the collector surface, and diffuse horizontal irradiance (DHI), light scattered by the atmosphere coming from all directions incident on a horizontal surface.

The impact of TT reflection on bifacial PV performance varies with sun position and sky condition, resulting in a dependence on the time of day and time of year. The irradiance gain due to TT reflection on the central collector is organized into sun zenith angle bins of 10°, with backtracking timestamps excluded to illustrate the trend of TT reflection decreasing with increasing sun zenith (Fig. 2). During backtracking timestamps, TT reflection makes a larger relative contribution to the irradiance due to the front-side cosine and angle of incidence losses. The irradiance gain is defined as the annual TT reflection in a zenith bin divided by the number of non-zero-GHI timestamps in that zenith bin. It is calculated per sample point, yielding an annual average 2D irradiance profile for each sun zenith bin. We analyze these trends using zenith instead of time of day to better represent a consistent illumination condition across the year. There is no 0-10° bin because this condition did not occur in Livermore. Timestamps with sun zenith greater than 80° were excluded from the analysis due to low incident irradiance.

The TT reflection is localized near the TT and strongest at low zeniths for both the 1P (Fig. 2b), and 2P (Fig. 2d) central collector. The absolute change in irradiance due to the TT reflection decreases with increasing zenith for both systems because GHI is greatest at solar noon. In a system with higher albedo or TT reflectivity, the impact of TT reflection would increase. Note the difference in color scales between the 1P and 2P configurations, with the 2P system's TT reflection being larger due to front-side illumination incident on the TT.

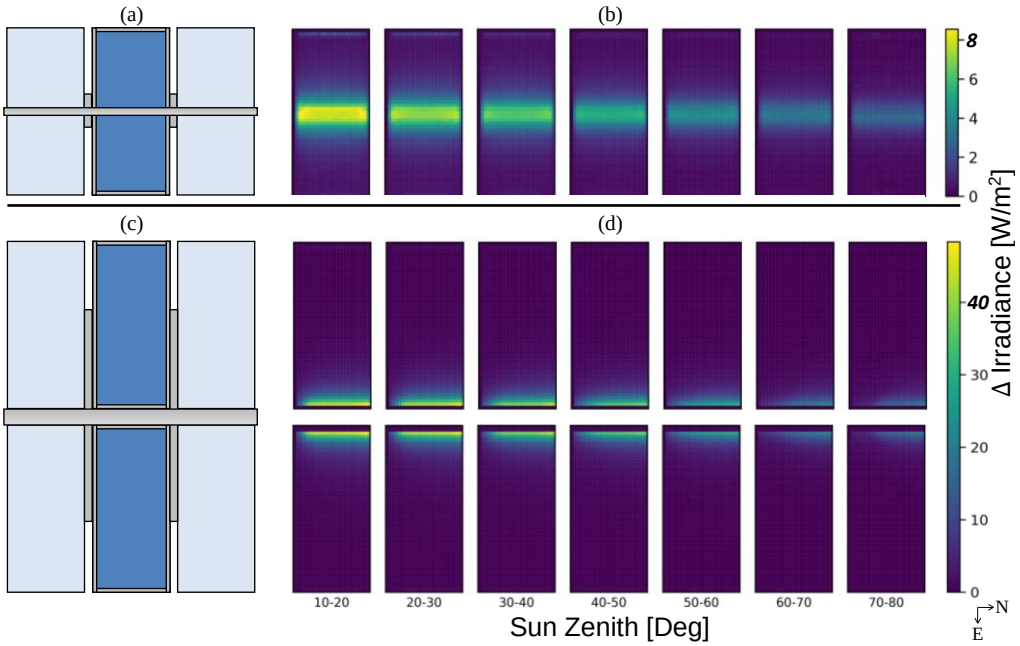

Fig. 2. Annual average change in irradiance on the rear of central collector due to TT reflection at different sun zenith angles for the (a, b) 1P system, and (c, d) 2P system. Frame widths, purlin widths, and module column gap along row are not to scale. Note the different irradiance scales.

The frame shades the collector from the TT reflection along the edges of the module(s). This is most evident on the module edges adjacent and parallel to the TT in the 2P collector (Fig. 2d), but is also visible along the north and south collector edges. Purlins also contribute to this effect because, as Livermore is in the northern hemisphere, the southern purlins partially block light incident on the TT, decreasing the TT reflection at the southern edge of the collector.

The irradiance maps in Fig. 2 show that the TT reflection decreases with increasing zenith but do not differentiate between sunny and cloudy sky conditions. In Fig. 3a and Fig. 3b, we report the annual average TT reflection over the central collector, $\bar{G}_{\mathrm{TT}_{\theta,d}}$ for each combination of zenith, θ, in bins of 10°, and DHI fraction, d, (defined as DHI/GHI), in bins of 0.1. $\bar{G}_{\mathrm{TT}_{\theta,d}}$ is calculated for each zenith and DHI fraction bin, and defined as the annual TT reflection in a zenith and DHI fraction bin divided by the number of non-zero-GHI timestamps in that bin. Instead of being calculated per sample point, it also condenses the TT reflection profile down to a single per-collector average for each zenith and DHI fraction bin (Fig. 3a and Fig. 3b). The TT reflection is greater in the 2P system due to the TT gap, and greatest during low DHI fraction and zenith bins due to the high GHI. The white spaces in Fig. 3, and dark grey spaces in Fig. 4, indicate zenith and DHI fraction combinations that did not occur at the test site. Due to the significant difference in irradiation conditions, the data is separated into regular tracking hours (the wide left subplots) and backtracking hours (the narrow right subplots). Regular tracking and backtracking hours include timestamps with zeniths greater than 60°, despite the maximum tracker angle of 60°, because, depending on the time of year, the sun's azimuth angle can make backtracking to avoid row-to-row shading unnecessary.

We also calculate the *relative* change in rear irradiance due to TT reflection for each zenith and DHI fraction bin,

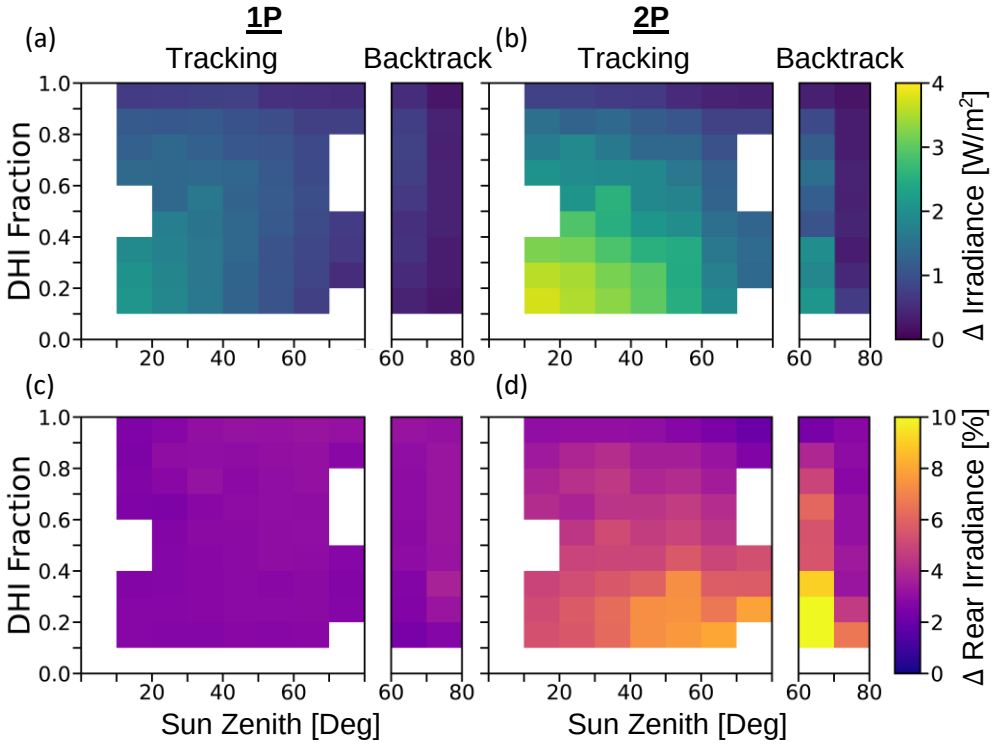

Fig. 3. Annual average collector irradiance due to the TT reflection as a function of sun zenith angle and DHI fraction for (a) 1P and (b) 2P systems. Annual average relative change in collector rear irradiance due to TT reflection for (c) 1P and (d) 2P systems as a function of sun zenith angle and DHI fraction

$$\bar{G}_{\mathrm{TTrel}_{\theta,d}} = \frac{\bar{G}_{\mathrm{TT}_{\theta,d}}}{\bar{G}_{\mathrm{TTA}_{\theta,d}}} \tag{2}$$

where $\bar{G}_{\mathrm{TTA}_{\theta,d}}$ is the annual average rear irradiance over a central module with an absorptive TT for a given zenith and DHI fraction bin. $\bar{G}_{\mathrm{TTrel}_{\theta,d}}$ increases the 1P system's central collector rear irradiance by an average of 2.8%, with little variation with respect to zenith and DHI fraction, and the greatest change coming at high DHI and zeniths (Fig. 3c). Conversely, in the 2P system (Fig. 3d), $\bar{G}_{\mathrm{TTrel}_{\theta,d}}$ increases with decreasing DHI fraction because of the direct beam light's contribution to the TT reflection. In addition, $\bar{G}_{\mathrm{TTrel}_{\theta,d}}$ in the 2P system is larger for high zenith timestamps because the baseline rear irradiance is smaller. This smaller baseline irradiance is the principal reason for the 2P system's backtracking timestamps showing the largest relative change in rear irradiance due to TT reflection, up to 10%.

3.2 Electrical mismatch

Cell-to-module electrical mismatch,

$$M_{\mathrm{cm}} = 1 - \frac{P_{\mathrm{mod}}}{\sum_{c=1}^{N} P_{\mathrm{cell},c}} \tag{3}$$

is the relative difference between the sum of cell maximum power points (P_{cell}) for all N cells in the module, and the maximum power point of the module (P_{mod}). Unlike uniform illumination conditions, where the current and voltage of cells are identical, nonuniform illumination leads to uneven current generation between cells, as seen in Fig. 9 of [7], reducing the current extracted from their series connection. The cell-to-module electrical mismatch

quantifies the impact of the irradiance nonuniformity over the module, providing the power loss due to current mismatch in the module. We will refer to cell-to-module electrical mismatch as simply the *electrical mismatch*.

TT reflection reduces electrical mismatch for *all* zenith and DHI fraction combinations in the 1P system (Fig. 4a) and *most* combinations in the 2P system (Fig. 4b). The decrease in electrical mismatch is due to the localization of the TT reflection near the TT partially offsetting TT shading. The TT reflection can reduce instantaneous electrical mismatch in the 1P and 2P system by up to 0.55% and 0.24% absolute, respectively, during high DHI fractions and zeniths, particularly at the onset of backtracking when the TT reflection and rear contribution to total irradiance are greatest.

TT reflection can *increase* electrical mismatch for the 2P module closest to the ground (Lower Module) at high zeniths (see Appendix C). While the additional irradiance from TT reflection is similar for both the Lower Module and its counterpart further from the ground (Upper Module), the Upper Module is preferentially shaded by the TT during timestamps with zeniths greater than 50°, see Fig. 1d for visual reference. There is therefore little shading on the Lower Module to offset during these timestamps and the additional irradiance from the TT reflection increases the irradiance nonuniformity, increasing the Lower Module's electrical mismatch for zeniths greater than 50° by ~0.02% on average. Conversely, TT reflection reduces electrical mismatch during all timestamps for the Upper Module because the TT reflection partially offsets the TT shading. Irradiance nonuniformity can also arise from brightening. This is apparent, for example, where TT reflection *increases* the Lower Module's electrical mismatch at high zeniths (see Appendix C). Despite the increased mismatch, the TT reflection still increases energy yield by increasing incident irradiance.

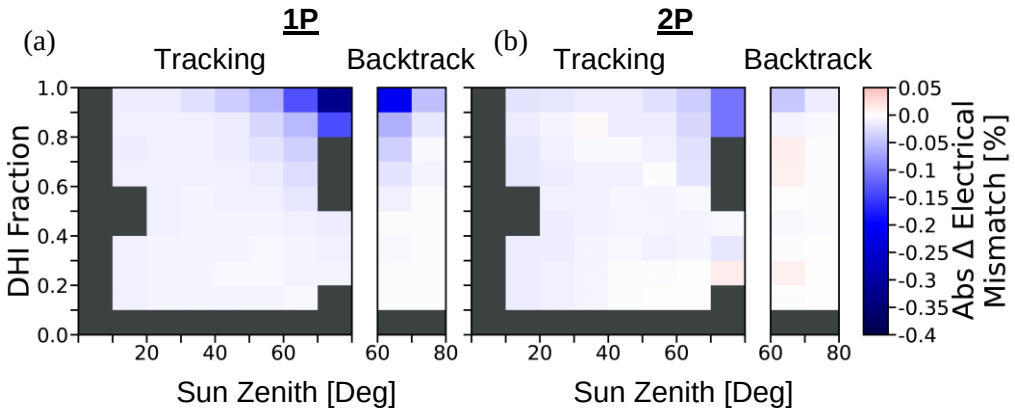

Fig. 4. Annually averaged absolute difference in cell-to-module electrical mismatch between absorptive and reflective TT as a function of sun zenith angle and DHI fraction in (a) 1P and (b) 2P single-axis tracked systems. Negative values indicate a reduction in electrical mismatch due to TT reflections. Dark grey squares indicate DHI fraction and sun zenith angle combinations that did not occur at the test site.

3.3 Energy yield

Similar to Fig. 3a and Fig. 3b, we calculate the average *absolute* change in energy yield due to TT reflection over the central collector for a given zenith and DHI fraction bin, $\bar{E}_{\mathrm{TT}_{\theta,d}}$. We also calculate the *relative* change in energy yield due to TT reflection given by

$$\bar{E}_{\mathrm{TTrel}_{\theta,d}} = \frac{\bar{E}_{\mathrm{TT}_{\theta,d}}}{\bar{E}_{\mathrm{TTA}_{\theta,d}}} \quad (4)$$

where $\bar{E}_{\mathrm{TTA}_{\theta,d}}$ is the annual average energy yield over a central module with an absorptive TT for a given zenith and DHI fraction bin. For both 1P and 2P systems, $\bar{E}_{\mathrm{TT}_{\theta,d}}$ is greatest during low DHI fractions with low zeniths because GHI is greatest under those conditions (Fig. 5a and Fig. 5b, respectively).

For the 1P system, $\bar{G}_{\mathrm{TTrel}_{\theta,d}}$ (Fig. 3c) is greatest during *high* DHI fractions and zeniths, and the TT reflection's impact is compounded when considering its change to *total* (front and rear) *energy yield*, $\bar{E}_{\mathrm{TTrel}_{\theta,d}}$, (Fig. 5c). The TT reflection reduces electrical mismatch, and the baseline energy yield without TT reflection is smaller at high DHI fractions and zeniths. During regular tracking, $\bar{E}_{\mathrm{TTrel}_{\theta,d}}$ ranges from 0.07% for low DHI fractions and zeniths, and up to 0.8% for high DHI fractions and zeniths. Similarly, during backtracking $\bar{E}_{\mathrm{TTrel}_{\theta,d}}$ranges from 0.03% to 0.6%.

For the 2P system, $\bar{G}_{\mathrm{TTrel}_{\theta,d}}$ (Fig. 3d) is greatest during *low* DHI fractions with high zeniths. However, both the TT reflection contribution to *total energy yield,* $\bar{E}_{\mathrm{TTrel}_{\theta,d}}$, (Fig. 5d), and the rear contribution are most significant at *high* DHI fractions with high zeniths due to less optimal conditions for front-incident light. During regular tracking, $\bar{E}_{\mathrm{TTrel}_{\theta,d}}$ ranges from 0.17% for low DHI fractions and up to 0.4% for high DHI fractions and zeniths. Similarly, during backtracking $\bar{E}_{\mathrm{TTrel}_{\theta,d}}$ ranges from 0.04% to 0.34%.

The maximum $\bar{E}_{\mathrm{TTrel}_{\theta,d}}$ occurs during high DHI fractions with high zeniths for both the 1P and 2P systems. It is notably higher in the 1P system despite the 2P system's larger absolute

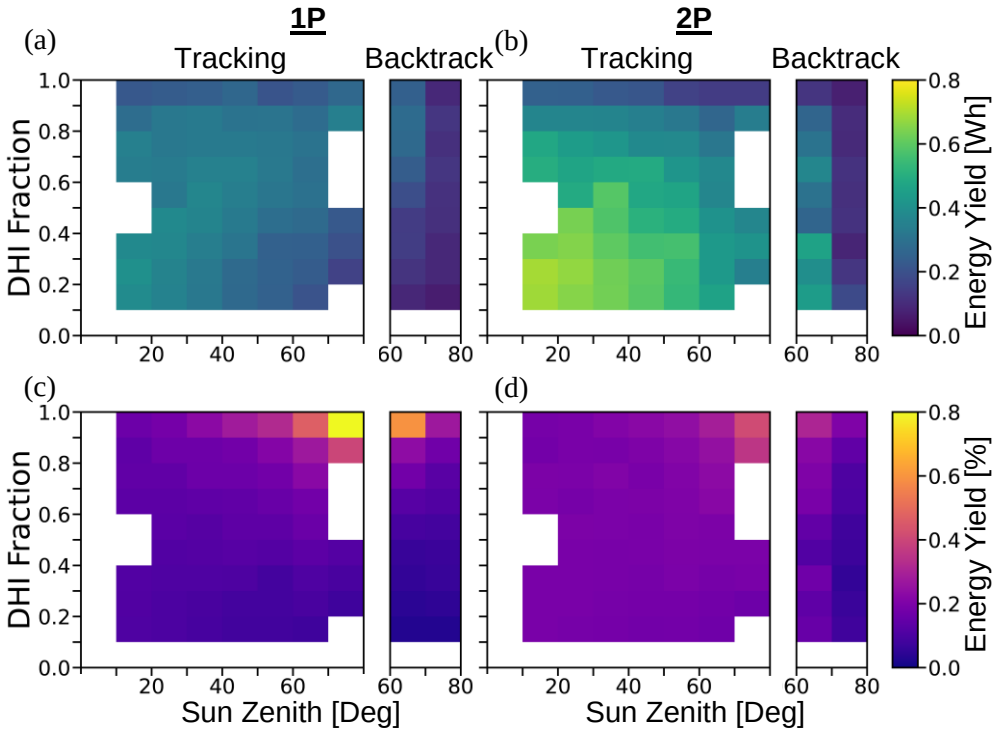

Fig. 5. Average difference in total energy yield due to TT-reflected light as a function of sun zenith angle and DHI fraction in (a, c) 1P and (b, d) 2P single-axis tracked systems. Change in total energy yield is absolute (a, b) and relative (c, d).

change in irradiance due to TT reflection. Therefore, the TT reflection's relative contribution to energy yield is greatest during less optimal conditions for front-incident light.

Table 1 reports the average impact of TT reflection on the central collector (per module for the 2P system) across all non-zero-GHI hours in the year. The TT reflection increases insolation, the time-integrated irradiance equivalent, by 0.17% and 0.30% in the 1P and 2P system, respectively. The TT reflection marginally reduces absolute electrical mismatch in both the 1P system and the 2P system. However, the 1P system's large baseline electrical mismatch (see Appendix D) results in a smaller relative reduction in electrical mismatch due to TT reflection compared to the 2P system. Overall, TT reflection increases total energy yield by 0.11% and 0.18% for the 1P and 2P system, respectively. While the TT reflection has a smaller impact on the 1P system in most conditions, the TT reflection's maximum *instantaneous* relative contribution to total energy yield is greater for the 1P system than the 2P system, at 0.8% and 0.4%, respectively.

Despite TT reflection decreasing electrical mismatch, the relative change in energy yield is less than the relative change in insolation. As shown in Fig. 2, the TT-reflected light incident on the collector is localized near the TT, meaning not all the additional irradiance will yield additional energy. The TT reflection may be nonuniform, but it partially offsets TT shading, resulting in a net benefit to electrical mismatch. A point on the module near the TT could go from one of the most shaded regions on the module to one of the most irradiated regions when comparing an absorptive and reflective TT.

Table 1. Annual Impact of TT reflection for Livermore, California, USA. Difference between the reflective TT and absorptive TT cases.

System	Collector Insolation			Electrical Mismatch		Bifacial Energy Yield	
	Abs Diff [kWh/m^2]	Rel Rear Diff [%]	Rel Total Diff [%]	Abs Diff [%]	Rel Diff [%]	Abs Diff [kWh/m^2]	Rel Diff [%]
1P	4.0	3.0	0.17	-0.008	-7.1	0.46	0.11
2P*	7.2	5.8	0.30	-0.007	-12.2	0.76	0.18

Diff: reflective TT result minus absorptive TT result
Abs: absolute
Rel: relative
* 2P values are reported as the average of the east and west central module pair

4. Conclusions

In this work, we applied TT reflection ray tracing calculations from bifacial_radiance to analyze its performance impact in DUET, a 3D view factor model with detailed shading, over an hourly typical meteorological year for the central 1P and 2P collector of single-axis tracked systems in Livermore, California, USA. We have quantified the effect of IAM on the TT reflection, yielding a larger relative impact than other rear-incident light due to its high average AOI. We identified that TT reflection reduces electrical mismatch by partially offsetting TT shading and, for an albedo of 0.2, TT reflection increases annual irradiance by 0.17% and 0.30% in the 1P and 2P system, respectively, leading to an increase in annual energy yield of 0.11% and 0.18%. The TT reflection is most significant when modelling instantaneous performance, increasing energy yield by up to 0.8% and 0.4% during high DHI fractions and sun zenith angles in the 1P and 2P system, respectively. While the overall impact of TT reflection is greater in the 2P system, the TT reflection's maximum instantaneous relative contribution to total energy yield is greater in the 1P system, at high DHI fractions and zeniths. The importance of including TT reflection in system simulations, therefore, depends upon the system type (1P vs 2P) and whether total or instantaneous energy yields are required.

Appendix A: Modeling parameters

Table 2 lists the geometric parameters used in the simulations. In bifacial_radiance simulations to isolate TT reflection, the reflectivity of the purlins, frame and TT are all set to 0.745. Then,

the TT reflectivity is changed to 0 while the reflectivity of the purlins and frame stays at 0.745. In DUET simulations, the reflectivity of all racking components is 0 and the TT reflection signal isolated from bifacial_radiance is added to the rear irradiance profile as a new irradiance source.

Table 2. Geometric parameters of the modeled arrays

Parameter	1P system	2P system
System configuration:		
Modules per row	23	
Number of rows	5	
Row pitch	4.8355 m	10 m
Ground cover ratio	0.456	
Piles	Not included	
Ground clearance	1.35 m	2.35 m
Tracking angle	±60°	
Module:		
Length	2.205 m	
Width	1.032 m	
Thickness	0.02 m	
Module gap	0.03 m	
Frame:		
Length	Module edge	
Width	0.011 m	
Thickness	0.03 m	
Purlins:		
Length	0.44 m	2.8 m
Width	0.03 m	
Thickness	0.08 m	
Torque tube:		
Torque tube gap	N/A	0.15 m
Shape	Round	
Diameter	0.1 m	0.2068 m
Reflectivity	0.745 or 0	
Specularity	0.9	
Roughness	0.2	

Appendix B: Incidence angle modifier impact on TT reflection

The incidence angle modifier (IAM), applied here using the ASHRAE model [43], accounts for angle-dependent reflection from the module. The IAM is calculated as

$$\mathrm{IAM} = 1 - b(\sec(\theta_{\mathrm{AOI}}) - 1) \tag{5}$$

where b is a parameter typically on the order of 0.05, and θ_{AOI} is the angle of incidence [38].

In the baseline system with an absorptive TT, applying the collector's IAM decreases the annual energy yield contributed by rear-incident light by 5.2% and 4.7% in the 1P and 2P systems, respectively. When applying the IAM to light from a reflective TT, the energy contributed by the TT reflection reduces by 7.4% and 8.4% for each system. This higher relative impact compared to other rear incident light is a result of the higher incidence angles between the TT and collector rear face.

Nonetheless, annual energy yield losses due to application of the IAM to the TT reflection remain small at just 0.008% and 0.016% in the 1P and 2P system, respectively, because the TT reflection itself contributes at most 0.8% of the energy yield for timestamps with zenith less than 80°. Considering all illumination sources, the IAM only decreases annual bifacial energy yield by 1.8% for both systems because the tracker minimizes the front-side incidence angle losses throughout the day. For completeness, we include the IAM for all irradiance sources, including TT-reflected light, throughout all our analyses herein.

Appendix C: TT reflection impact on 2P upper and lower module

The TT reflection impact on electrical mismatch differs between the 2P system's central module closer to the ground (Lower Module), and the module further from the ground (Upper Module) (Fig. 6a and b, respectively). The TT reflection can increase electrical mismatch on the Lower Module (Fig. 6a) during high zeniths by up to 0.04% absolute, most of all during backtracking timestamps with high sun zenith angle. In contrast, the TT reflection decreases electrical mismatch on the Upper Module (Fig. 6b) for all DHI fraction and zenith combinations.

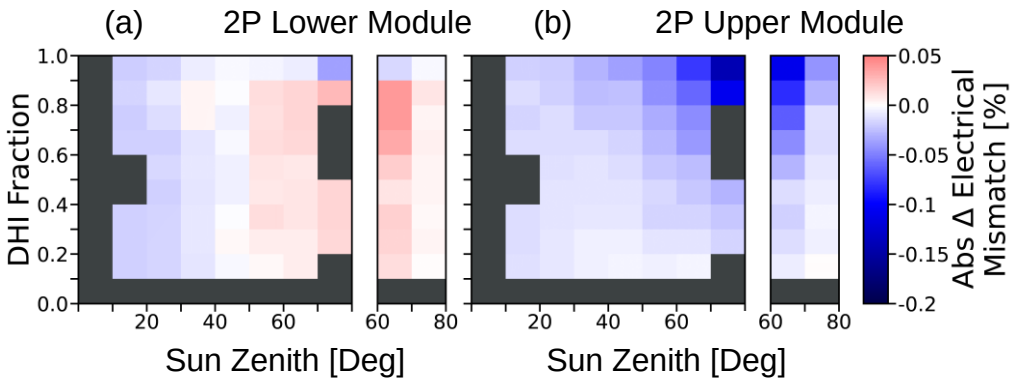

Fig. 6. Average absolute variation in cell-to-module level electrical mismatch due to TT reflection for the (a) 2P lower module and (b) 2P upper module. Charcoal black squares indicate DHI fraction and sun zenith angle combinations that did not occur at the test site. Large left subplots exclude backtracking timestamps; the narrower right subplots include only backtracking timestamps.

Appendix D: Annual results for absorptive and reflective TT cases

Table 3 shows annual results for 1P and 2P systems with an absorptive torque tube (TTA) and a reflective torque tube (TTR). The differences between the reflective and absorptive TT values lead to the values in Table 1. They are presented here for convenience.

Table 3. Annual results for absorptive TT and reflective TT cases.

System	Collector Insolation [kWh/m^2]		Electrical Mismatch [%]	Bifacial Energy Yield [kWh/m^2]
	Rear	Total		
1P TTA	133.13	2354.25	0.108	431.31
1P TTR	137.10	2358.22	0.100	431.77
2P* TTA	123.06	2344.89	0.060	430.62
2P* TTR	130.21	2352.04	0.053	431.38

TTA: results from simulations with an absorptive TT
TTR: results from simulations with a reflective TT
* 2P values are reported as the average of the east and west central module pair

Funding. The authors thank Natural Sciences and Engineering Research Council of Canada (STPGP 521894-18, RGPIN-2022-03877, RGPIN-2015-04782, NSERC CREATE 497981, NSERC CGS-M, CGS-D, PGS-D) for financial support.

Disclosures. The authors declare no conflicts of interest.

Data availability. Data underlying the results presented in this paper are not publicly available at this time but may be obtained from the authors upon reasonable request.

Acknowledgement. The authors would like to thank Javier Guerrero Pérez, Mireia Jiménez Beltran, and Alejandro Conesa from Soltec Innovations for their correspondence regarding the Livermore test site, the Soltec SF7 tracker, and insightful discussions.

References

1. C. D. Rodríguez-Gallegos, H. Liu, O. Gandhi, J. P. Singh, V. Krishnamurthy, A. Kumar, J. S. Stein, S. Wang, L. Li, T. Reindl, and I. M. Peters, "Global Techno-Economic Performance of Bifacial and Tracking Photovoltaic Systems," Joule **4**(7), 1514–1541 (2020).
2. M. Koussa, A. Cheknane, S. Hadji, M. Haddadi, and S. Noureddine, "Measured and modelled improvement in solar energy yield from flat plate photovoltaic systems utilizing different tracking systems and under a range of environmental conditions," Appl. Energy **88**(5), 1756–1771 (2011).
3. C. Olalla, C. Deline, and D. Maksimovic, "Performance of mismatched PV systems with submodule integrated converters," IEEE J. Photovoltaics **4**(1), 396–404 (2014).
4. C. Deline, S. Ayala Pelaez, S. MacAlpine, and C. Olalla, "Estimating and parameterizing mismatch power loss in bifacial photovoltaic systems," Prog. Photovoltaics Res. Appl. **28**(7), 691–703 (2020).
5. K. A. K. Niazi, Y. Yang, and D. Sera, "Review of mismatch mitigation techniques for PV modules," IET Renew. Power Gener. **13**(12), 2035–2050 (2019).
6. K. R. McIntosh, M. D. Abbott, G. Loomis, B. A. Sudbury, A. Mayer, C. Zak, and J. Meydbrey, "Irradiance on the upper and lower modules of a two-high bifacial tracking system," Conf. Rec. IEEE Photovolt. Spec. Conf. (IEEE, 2020), pp. 1916–1923.
7. K. R. McIntosh, M. D. Abbott, B. A. Sudbury, and J. Meydbray, "Mismatch Loss in Bifacial Modules Due to Nonuniform Illumination in 1-D Tracking Systems," IEEE J. Photovoltaics **9**(6), 1504–1512 (2019).
8. C. Olalla, M. N. Hasan, C. Deline, and D. Maksimović, "Mitigation of hot-spots in photovoltaic systems using distributed power electronics," Energies **11**(4), 1–16 (2018).
9. R. Kopecek and J. Libal, "Towards large-scale deployment of bifacial photovoltaics," Nat. Energy **3**(6), 443–446 (2018).
10. S. A. Pelaez, C. Deline, P. Greenberg, J. S. Stein, and R. K. Kostuk, "Model and Validation of Single-Axis Tracking with Bifacial PV," IEEE J. Photovoltaics **9**(3), 715–721 (2019).
11. S. A. Pelaez and C. Deline, "Bifacial_Radiance: a Python Package for Modeling Bifacial Solar Photovoltaic Systems," J. Open Source Softw. **5**(50), 1865 (2020).
12. S. A. Pelaez, C. Deline, S. M. Macalpine, B. Marion, J. S. Stein, and R. K. Kostuk, "Comparison of Bifacial Solar Irradiance Model Predictions with Field Validation," IEEE J. Photovoltaics **9**(1), 82–88 (2019).
13. K. R. McIntosh, M. D. Abbott, B. A. Sudbury, J. Nagyvary, K. Lee, L. Creasy, J. Sharp, J. Crimmins, and D. Zirzow, "Simulation and measurement of monofacial and bifacial modules in a 1D tracking system," Conf. Rec. IEEE Photovolt. Spec. Conf. (IEEE, 2020), pp. 0366–0370.
14. C. K. Lo, Y. S. Lim, and F. A. Rahman, "New integrated simulation tool for the optimum design of bifacial solar panel with reflectors on a specific site," Renew. Energy **81**, 293–307 (2015).
15. A. Asgharzadeh, M. A. Anoma, A. Hoffman, C. Chaudhari, S. Bapat, R. Perkins, D. Cohen, G. M. Kimball, D. Riley, F. Toor, and B. Bourne, "A Benchmark and Validation of Bifacial PV Irradiance Models," Conf. Rec. IEEE Photovolt. Spec. Conf. (IEEE, 2019), pp. 3281–3287.
16. C. Zhao, J. Xiao, Y. Yu, and J.-N. Jaubert, "Accurate shading factor and mismatch loss analysis of bifacial HSAT systems through ray-tracing modeling," Sol. Energy Adv. **1**, 100004 (2021).
17. M. Ernst, G. E. J. Conechado, and C. A. Asselineau, "Accelerating the simulation of annual bifacial illumination of real photovoltaic systems with ray tracing," iScience **25**(1), 103698 (2022).
18. J. R. Ledesma, R. H. Almeida, F. Martinez-Moreno, C. Rossa, J. Martín-Rueda, L. Narvarte, and E. Lorenzo, "A simulation model of the irradiation and energy yield of large bifacial photovoltaic plants," Sol. Energy **206**, 522–538 (2020).
19. B. Marion, S. MacAlpine, C. Deline, A. Asgharzadeh, F. Toor, D. Riley, J. Stein, and C. Hansen, "A Practical Irradiance Model for Bifacial PV Modules," in *IEEE 44th Photovolt. Spec. Conf.* (IEEE, 2017), pp. 1537–1542.
20. M. A. Anoma, D. Jacob, B. C. Bourne, J. A. Scholl, D. M. Riley, and C. W. Hansen, "View Factor Model and Validation for Bifacial PV and Diffuse Shade on Single-Axis Trackers," in IEEE 44th Photovolt. Spec. Conf. (IEEE, 2017), pp. 1549–1554.
21. D. Berrian, J. Libal, M. Klenk, H. Nussbaumer, and R. Kopecek, "Performance of Bifacial PV Arrays with Fixed Tilt and Horizontal Single-Axis Tracking: Comparison of Simulated and Measured Data," IEEE J. Photovoltaics **9**(6), 1583–1589 (2019).
22. C. D. Rodríguez-Gallegos, M. Bieri, O. Gandhi, J. P. Singh, T. Reindl, and S. K. Panda, "Monofacial vs bifacial Si-based PV modules: Which one is more cost-effective?," Sol. Energy **176**, 412–438 (2018).
23. M. Rouholamini, L. Chen, and C. Wang, "Modeling, Configuration, and Grid Integration Analysis of Bifacial PV Arrays," IEEE Trans. Sustain. Energy **12**(2), 1242–1255 (2021).
24. P. Gilman, A. Dobos, N. DiOrio, J. Freeman, S. Janzou, and D. Ryberg, "System Advisor Model (SAM) Photovoltaic Model Technical Reference Update," Natl. Renew. Energy Lab., 93 (2018).
25. B. Wittmer, "Simulating Bifacial Fixed Tilt and Tracking Systems with PVsyst," PV Mag. Webinar (2019).
26. W. Gu, T. Ma, M. Li, L. Shen, and Y. Zhang, "A coupled optical-electrical-thermal model of the bifacial photovoltaic module," Appl. Energy **258**, 114075 (2020).
27. E. G. D. Barros, B. B. Van Aken, A. R. Burgers, L. H. Slooff-Hoek, and R. M. Fonseca, "Multi-Objective optimization of solar park design under climatic uncertainty," Sol. Energy **231**, 958–969 (2022).
28. U. A. Yusufoglu, T. H. Lee, T. M. Pletzer, A. Halm, L. J. Koduvelikulathu, C. Comparotto, R. Kopecek,

and H. Kurz, "Simulation of energy production by bifacial modules with revision of ground reflection," Energy Procedia **55**, 389–395 (2014).
29. D. Chudinzow, J. Haas, G. Díaz-Ferrán, S. Moreno-Leiva, and L. Eltrop, "Simulating the energy yield of a bifacial photovoltaic power plant," Sol. Energy **183**, 812–822 (2019).
30. M. A. Mikofski, R. Darawali, M. Hamer, A. Neubert, and J. Newmiller, "Bifacial Performance Modeling in Large Arrays," Conf. Rec. IEEE Photovolt. Spec. Conf. (1), 1282–1287 (2019).
31. A. C. J. Russell, C. E. Valdivia, C. Bohémier, J. E. Haysom, and K. Hinzer, "DUET : A Novel Energy Yield Model With 3D Shading for Bifacial Photovoltaic Systems," IEEE J. Photovoltaics 1–10 (2022).
32. D. Berrian and J. Libal, "A comparison of ray tracing and view factor simulations of locally resolved rear irradiance with the experimental values," Prog. Photovoltaics Res. Appl. **28**(6), 609–620 (2020).
33. N. Riedel-lyngskær, D. Berrian, D. A. Mira, A. A. Protti, P. B. Poulsen, J. Libal, and J. Vedde, "Validation of bifacial photovoltaic simulation software against monitoring data from large-scale single-axis trackers and fixed tilt systems in Denmark," Appl. Sci. **10**(23), 1–29 (2020).
34. J. S. Stein, C. Reise, J. B. Castro, G. Friesen, G. Maugeri, E. Urrejola, and S. Ranta, "Bifacial PV modules & Systems: Experience and Results from International Research and Pilot Applications," (International Energy Agency Photovoltaic Power Systems Programme, 2021). https://iea-pvps.org/wp-content/uploads/2021/04/IEA-PVPS-T13-14_2021-Bifacial-Photovoltaic-Modules-and-Systems-report.pdf.
35. J. Guerrero-Perez, A. C. J. Russell, C. E. Valdivia, A. Conesa, T. J. Coathup, M. R. Lewis, I. Munoz, and K. Hinzer, "Bifacial PV Modules Shading and Mismatch Impact on Yearly Energy Yield simulations," in Photovolt. Sci. and Eng. Conf. (2021).
36. T. Coathup, M. R. Lewis, A. C. J. Russell, A. Conesa, J. Guerrero-Perez, C. E. Valdivia, and K. Hinzer, "Impact of reflective torque tube on rear side irradiance in bifacial photovoltaic modules," Proc. SPIE 11996, 119960A (2022).
37. X. Sun, M. R. Khan, C. Deline, and M. A. Alam, "Optimization and performance of bifacial solar modules: A global perspective," Appl. Energy **212**, 1601–1610 (2018).
38. W. F. Holmgren, R. W. Andrews, A. T. Lorenzo, and J. S. Stein, "PVLIB Python 2015," in IEEE 42nd Photovolt. Spec. Conf., (IEEE, 2015), pp. 1–5.
39. Jinko S Solar, Tiger Bifacial DG module datasheet, https://jinkosolar.eu/.
40. M. Sengupta, Y. Xie, A. Lopez, A. Habte, G. Maclaurin, and J. Shelby, "The National Solar Radiation Data Base (NSRDB)," Renew. Sustain. Energy Rev. **89**, 51–60 (2018).
41. G. W. Larson and R. A. Shakespeare, *Rendering with Radiance: The Art and Science of Lighting Visualization* (Morgan Kaufmann Publishers, 1998).
42. S. A. Pelaez, C. Deline, J. S. Stein, B. Marion, K. Anderson, and M. Muller, "Effect of torque-tube parameters on rear-irradiance and rear-shading loss for bifacial PV performance on single-axis tracking systems," in Conference Record of the IEEE Photovolt. Spec. Conf. (2019), **2**, pp. 3525–3530.
43. A. F. Souka and H. H. Safwat, "Determination of the optimum orientations for the double-exposure, flat-plate collector and its reflectors," Sol. Energy **10**(4), 170–174 (1966).

Chapter 5: Conclusions

5.1 Conclusion

This thesis investigated the impact of including TT reflection in horizontal single-axis tracked bifacial PV performance modeling. Bifacial PV are a promising technology poised to overtake the majority of the PV market share in the next ten years. Accurate performance models with high computational throughput will further hasten their adoption by reducing investor uncertainty and optimizing PV array designs. Our study began by isolating the irradiance reflecting off the TT that is incident on the module rear face of 1P and 2P horizontal single-axis tracked systems. In section 3.2, an arbitrary 2D irradiance sampling method was implemented in bifacial_radiance along with racking elements that track with the modules. We found that TT reflection partially offsets TT shading in 1P and 2P horizontal single-axis tracked systems, increasing annual rear insolation by 3% and 5.5%, respectively, and reducing rear-side insolation mismatch by 1.1% and 1.5%, respectively, for 0.2 albedo. We also established that TT shading and reflection impacts vary over the course of a day and year.

In section 4.2, we expanded on the idea that TT reflection varies over the course of a day and year by analyzing its impact as a function of DHI fraction and sun zenith. We incorporated the TT reflection as an additional light source in DUET, with an incidence angle modifier, to analyze its performance impact on irradiance, electrical mismatch and energy yield. We identified that TT reflection reduces electrical mismatch in both 1P and 2P systems, and increases annual energy yield by 0.11% and 0.18%, respectively. However, the TT reflection is most significant when modeling instantaneous performance, increasing energy yield by up to 0.8% and 0.4% during high DHI fractions and sun zenith angles in the 1P and 2P systems, respectively.

5.2 Further Research

This section presents recommendations for extensions of the work.

First, we recommend comparing simulation results with and without TT reflection to experimental data with and without TT reflection, captured side-by-side to isolate the TT reflection. Validating simulations against experimental data is the only true way of determining if incorporating TT reflection increases or decreases modelling accuracy. This could be done with either a calibrated indoor or outdoor PV system. Indoor testing would require specific data points for

calibrating to outdoor results for one or two data point across the year. Outdoor monitoring would require one week to one year for sufficient validation.

The simulation method for isolating the impact of TT reflection can also be used to help inform TT manufacturers of new designs to minimize electrical mismatch and maximize energy yield. For instance, given minimum mechanical strength benchmarks, TT size, shape, and reflectivity can be optimized. The results may also vary based on site latitude and albedo. As such, we recommend preforming simulations quantifying the impact of TT reflection at different latitude locations and at different albedo.

Not all bifacial PV performance models include TT reflection, but every opportunity should be taken to provide bifacial PV stakeholders with the tools to match their desired accuracy-specificity balance. This thesis recommends developing a method of calculating TT reflection natively within DUET, instead of relying on bifacial_radiance or other ray tracing tools to isolate the TT reflection. For example, future research could investigate treating the TT as a reflective surface, like the ground. This will increase computational throughput. The current method required each timestamp to be simulated four times: in bifacial_radiance with a reflective and absorptive TT, and in DUET with and without the additional TT reflection irradiance profile. The TT reflection simulations presented here are a starting point that can build towards a 3D view factor model with detailed shading and select reflections.

References

[1] C. D. Rodríguez-Gallegos, H. Liu, O. Gandhi, *et al.*, "Global Techno-Economic Performance of Bifacial and Tracking Photovoltaic Systems," *Joule*, vol. 4, no. 7, pp. 1514–1541, 2020, ISSN: 25424351. DOI: 10.1016/j.joule.2020.05.005.

[2] M. Koussa, A. Cheknane, S. Hadji, M. Haddadi, and S. Noureddine, "Measured and modelled improvement in solar energy yield from flat plate photovoltaic systems utilizing different tracking systems and under a range of environmental conditions," *Applied Energy*, vol. 88, no. 5, pp. 1756–1771, 2011, ISSN: 03062619. DOI: 10.1016/j.apenergy.2010.12.002.

[3] VDMA, *International Technology Roadmap for Photovoltaic (ITRPV)*, 2021. [Online]. Available: https://itrpv.vdma.org/en/ueber-uns.

[4] N. Riedel-lyngskær, D. Berrian, D. A. Mira, *et al.*, "Validation of bifacial photovoltaic simulation software against monitoring data from large-scale single-axis trackers and fixed tilt systems in Denmark," *Applied Sciences (Switzerland)*, vol. 10, no. 23, pp. 1–29, 2020, ISSN: 20763417. DOI: 10.3390/app10238487.

[5] J. S. Stein, C. Reise, J. B. Castro, *et al.*, *Bifacial PV modules systems: Experience and Results from International Research and Pilot Applications*, 2021. [Online]. Available: https://iea-pvps.org/wp-content/uploads/2021/04/IEA-PVPS-T13-14%5C_2021-Bifacial-Photovoltaic-Modules-and-Systems-report.pdf.

[6] A. Asgharzadeh, B. Marion, C. Deline, C. Hansen, J. S. Stein, and F. Toor, "A sensitivity study of the impact of installation parameters and system configuration on the performance of bifacial PV arrays," *IEEE Journal of Photovoltaics*, vol. 8, no. 3, pp. 798–805, 2018, ISSN: 21563381. DOI: 10.1109/JPHOTOV.2018.2819676.

[7] J. R. Ledesma, R. H. Almeida, F. Martinez-Moreno, *et al.*, "A simulation model of the irradiation and energy yield of large bifacial photovoltaic plants," *Solar Energy*, vol. 206, no. May, pp. 522–538, 2020, ISSN: 0038092X. DOI: 10.1016/j.solener.2020.05.108. [Online]. Available: https://doi.org/10.1016/j.solener.2020.05.108.

[8] B. Marion, S. MacAlpine, C. Deline, *et al.*, "A Practical Irradiance Model for Bifacial PV Modules," in *IEEE 44th Photovolt. Spec. Conf.*, IEEE, Jun. 2017, pp. 1537–1542, ISBN: 978-1-5090-5605-7. DOI: 10.1109/PVSC.2017.8366263. [Online]. Available: https://ieeexplore.ieee.org/document/8366263/.

[9] M. A. Anoma, D. Jacob, B. C. Bourne, J. A. Scholl, D. M. Riley, and C. W. Hansen, "View Factor Model and Validation for Bifacial PV and Diffuse Shade on Single-Axis Trackers," in *IEEE 44th Photovolt. Spec. Conf.*, IEEE, Jun. 2017, pp. 1549–1554, ISBN: 978-1-5090-5605-7. DOI: 10.1109/PVSC.2017.8366704. [Online]. Available: https://ieeexplore.ieee.org/document/8366704/.

[10] D. Berrian and J. Libal, "A comparison of ray tracing and view factor simulations of locally resolved rear irradiance with the experimental values," *Progress in Photovoltaics: Research and Applications*, vol. 28, no. 6, pp. 609–620, 2020, ISSN: 1099159X. DOI: 10.1002/pip.3261.

[11] S. A. Pelaez, C. Deline, P. Greenberg, J. S. Stein, and R. K. Kostuk, "Model and Validation of Single-Axis Tracking with Bifacial PV," *IEEE Journal of Photovoltaics*, vol. 9, no. 3, pp. 715–721, 2019, ISSN: 21563403. DOI: 10.1109/JPHOTOV.2019.2892872.

[12] K. R. McIntosh, M. D. Abbott, B. A. Sudbury, *et al.*, "Simulation and measurement of monofacial and bifacial modules in a 1D tracking system," *Conference Record of the IEEE Photovoltaic Specialists Conference*, vol. 2020-June, pp. 0366–0370, 2020, ISSN: 01608371. DOI: 10.1109/PVSC45281.2020.9300620.

[13] C. K. Lo, Y. S. Lim, and F. A. Rahman, "New integrated simulation tool for the optimum design of bifacial solar panel with reflectors on a specific site," *Renewable Energy*, vol. 81, pp. 293–307, 2015, ISSN: 18790682. DOI: 10.1016/j.renene.2015.03.047. [Online]. Available: http://dx.doi.org/10.1016/j.renene.2015.03.047.

[14] R. Kopecek and J. Libal, "Towards large-scale deployment of bifacial photovoltaics," Tech. Rep. 6, 2018, pp. 443–446. DOI: 10.1038/s41560-018-0178-0. [Online]. Available: https://doi.org/10.1038/s41560-018-0178-0.

[15] K. R. McIntosh, M. D. Abbott, B. A. Sudbury, and J. Meydbray, "Mismatch Loss in Bifacial Modules Due to Nonuniform Illumination in 1-D Tracking Systems," *IEEE Journal of Photovoltaics*, vol. 9, no. 6, pp. 1504–1512, 2019, ISSN: 21563403. DOI: 10.1109/JPHOTOV.2019.2937217.

[16] S. A. Pelaez, C. Deline, J. S. Stein, B. Marion, K. Anderson, and M. Muller, "Effect of torque-tube parameters on rear-irradiance and rear-shading loss for bifacial PV performance on single-axis tracking systems," in *Conference Record of the IEEE Photovoltaic Specialists Conference*, vol. 2, 2019, pp. 3525–3530, ISBN: 9781728104942. DOI: 10.1109/PVSC40753.2019.9198975.

[17] S. A. Pelaez, C. Deline, S. M. Macalpine, B. Marion, J. S. Stein, and R. K. Kostuk, "Comparison of Bifacial Solar Irradiance Model Predictions with Field Validation," *IEEE Journal of Photovoltaics*, vol. 9, no. 1, pp. 82–88, 2019, ISSN: 21563381. DOI: 10.1109/JPHOTOV.2018.2877000.

[18] S. A. Pelaez and C. Deline, "Bifacial_Radiance: a Python Package for Modeling Bifacial Solar Photovoltaic Systems," *Journal of Open Source Software*, vol. 5, no. 50, p. 1865, 2020, ISSN: 2475-9066. DOI: 10.21105/joss.01865.

[19] C. Zhao, J. Xiao, Y. Yu, and J.-N. Jaubert, "Accurate shading factor and mismatch loss analysis of bifacial HSAT systems through ray-tracing modeling," *Solar Energy Advances*, vol. 1, no. September, p. 100 004, 2021, ISSN: 26671131. DOI: 10.1016/j.seja.2021.100004. [Online]. Available: https://doi.org/10.1016/j.seja.2021.100004.

[20] M. Ernst, G. E. Conechado, and C. A. Asselineau, "Accelerating the simulation of annual bifacial illumination of real photovoltaic systems with ray tracing," *iScience*, vol. 25, no. 1, p. 103 698, 2022, ISSN: 25890042. DOI: 10.1016/j.isci.2021.103698. [Online]. Available: https://doi.org/10.1016/j.isci.2021.103698.

[21] D. Berrian, J. Libal, M. Klenk, H. Nussbaumer, and R. Kopecek, "Performance of Bifacial PV Arrays with Fixed Tilt and Horizontal Single-Axis Tracking: Comparison of Simulated and Measured Data," *IEEE Journal of Photovoltaics*, vol. 9, no. 6, pp. 1583–1589, 2019, ISSN: 21563403. DOI: 10.1109/JPHOTOV.2019.2924394.

[22] C. D. Rodríguez-Gallegos, M. Bieri, O. Gandhi, J. P. Singh, T. Reindl, and S. K. Panda, "Monofacial vs bifacial Si-based PV modules: Which one is more cost-effective?" *Solar Energy*, vol. 176, no. August, pp. 412–438, 2018, ISSN: 0038092X. DOI: 10.1016/j.solener.2018.10.012. [Online]. Available: https://doi.org/10.1016/j.solener.2018.10.012.

[23] M. Rouholamini, L. Chen, and C. Wang, "Modeling, Configuration, and Grid Integration Analysis of Bifacial PV Arrays," *IEEE Transactions on Sustainable Energy*, vol. 12, no. 2, pp. 1242–1255, 2021, ISSN: 19493037. DOI: 10.1109/TSTE.2020.3040427.

[24] P. Gilman, A. Dobos, N. DiOrio, J. Freeman, S. Janzou, and D. Ryberg, "System Advisor Model (SAM) Photovoltaic Model Technical Reference Update," *National Renewable Energy Laboratory*, no. March, p. 93, 2018. [Online]. Available: https://sam.nrel.gov/%5C%0Ahttps://sam.nrel.gov/images/web%5C_page%5C_files/sam-help-2018-11-11-r4.pdf%5C%0Asam.nrel.gov/content/downloads.

[25] B. Wittmer, "Simulating Bifacial Fixed Tilt and Tracking Systems with PVsyst," *PV Magazine Webinar*, 2019.

[26] W. Gu, T. Ma, M. Li, L. Shen, and Y. Zhang, "A coupled optical-electrical-thermal model of the bifacial photovoltaic module," *Applied Energy*, vol. 258, no. October 2019, p. 114 075, 2020, ISSN: 03062619. DOI: 10.1016/j.apenergy.2019.114075. [Online]. Available: https://doi.org/10.1016/j.apenergy.2019.114075.

[27] E. G. Barros, B. B. Van Aken, A. R. Burgers, L. H. Slooff-Hoek, and R. M. Fonseca, "Multi-Objective optimization of solar park design under climatic uncertainty," *Solar Energy*, vol. 231, no. April 2021, pp. 958–969, 2022, ISSN: 0038092X. DOI: 10.1016/j.solener.2021.12.026. [Online]. Available: https://doi.org/10.1016/j.solener.2021.12.026.

[28] U. A. Yusufoglu, T. H. Lee, T. M. Pletzer, *et al.*, "Simulation of energy production by bifacial modules with revision of ground reflection," *Energy Procedia*, vol. 55, pp. 389–395, 2014, ISSN: 18766102. DOI: 10.1016/j.egypro.2014.08.111. [Online]. Available: http://dx.doi.org/10.1016/j.egypro.2014.08.111.

[29] D. Chudinzow, J. Haas, G. Díaz-Ferrán, S. Moreno-Leiva, and L. Eltrop, "Simulating the energy yield of a bifacial photovoltaic power plant," *Solar Energy*, vol. 183, no. March, pp. 812–822, 2019, ISSN: 0038092X. DOI: 10.1016/j.solener.2019.03.071. [Online]. Available: https://doi.org/10.1016/j.solener.2019.03.071.

[30] M. A. Mikofski, R. Darawali, M. Hamer, A. Neubert, and J. Newmiller, "Bifacial Performance Modeling in Large Arrays," *Conference Record of the IEEE Photovoltaic Specialists Conference*, no. 1, pp. 1282–1287, 2019, ISSN: 01608371. DOI: 10.1109/PVSC40753.2019.8980572.

[31] A. C. J. Russell, C. E. Valdivia, C. Bohémier, J. E. Haysom, and K. Hinzer, "DUET : A Novel Energy Yield Model With 3D Shading for Bifacial Photovoltaic Systems," *IEEE Journal of Photovoltaics*, pp. 1–10, 2022. DOI: 10.1109/JPHOTOV.2022.3185546.

[32] C. Deline, S. Ayala Pelaez, S. MacAlpine, and C. Olalla, "Estimating and parameterizing mismatch power loss in bifacial photovoltaic systems," *Progress in Photovoltaics: Research and Applications*, vol. 28, no. 7, pp. 691–703, 2020, ISSN: 1099159X. DOI: 10.1002/pip.3259.

[33] J. Guerrero-Perez, A. C. J. Russell, C. E. Valdivia, *et al.*, "Bifacial PV Modules Shading and Mismatch Impact on Yearly Energy Yield simulations," in *PVSEC*, 2021.

[34] M. Sengupta, Y. Xie, A. Lopez, A. Habte, G. Maclaurin, and J. Shelby, "The National Solar Radiation Data Base (NSRDB)," *Renewable and Sustainable Energy Reviews*, vol. 89, no. January 2018, pp. 51–60, 2018, ISSN: 18790690. DOI: 10.1016/j.rser.2018.03.003. [Online]. Available: https://doi.org/10.1016/j.rser.2018.03.003.

[35] A. Louwen and W. van Sark, "Photovoltaic solar energy," in *Technological Learning in the Transition to a Low-Carbon Energy System*, Elsevier, 2020, pp. 65–86, ISBN: 9780128187623. DOI: 10.1016/B978-0-12-818762-3.00005-4. [Online]. Available: https://linkinghub.elsevier.com/retrieve/pii/B9780128187623000054.

[36] F. Kasten and A. T. Young, "Revised optical air mass tables and approximation formula," vol. 28, no. 22, pp. 4735–4738, 2000.

[37] A. International, *G173-03 Standard Tables for Reference Solar Spectral Irradiances: Direct Normal and Hemispherical on 37 Tilted Surface*, West Conshohocken, PA, 2012. DOI: 10.1520/G0173-03R12.

[38] C. A. Gueymard, *SMARTS2: a simple model of the atmospheric radiative transfer of sunshine: algorithms and performance assessment*, 1995. [Online]. Available: http://instesre.org/GCCE/SMARTS2.pdf.

[39] NREL, *Reference Air Mass 1.5 Spectra*. [Online]. Available: https://www.nrel.gov/grid/solar-resource/spectra-am1.5.html.

[40] W. Shockley and H. Queisser, "Detailed Balance Limit of Efficiency of p–n Junction Solar Cells," *Journal of Applied Physics*, vol. 32, no. 3, pp. 510–519, Mar. 1961. DOI: 10.4324/9781315793245-44. [Online]. Available: https://www.taylorfrancis.com/books/9781317740933/chapters/10.4324/9781315793245-44.

[41] C. Olalla, M. N. Hasan, C. Deline, and D. Maksimović, "Mitigation of hot-spots in photovoltaic systems using distributed power electronics," *Energies*, vol. 11, no. 4, pp. 1–16, 2018, ISSN: 19961073. DOI: 10.3390/en11040726.

[42] J. E. Castillo-Aguilella and P. S. Hauser, "Multi-Variable Bifacial Photovoltaic Module Test Results and Best-Fit Annual Bifacial Energy Yield Model," *IEEE Access*, vol. 4, pp. 498–506, 2016, ISSN: 21693536. DOI: 10.1109/ACCESS.2016.2518399.

[43] K. A. K. Niazi, Y. Yang, and D. Sera, "Review of mismatch mitigation techniques for PV modules," *IET Renewable Power Generation*, vol. 13, no. 12, pp. 2035–2050, 2019, ISSN: 17521424. DOI: 10.1049/iet-rpg.2019.0153.

[44] W. F. Holmgren, R. W. Andrews, A. T. Lorenzo, and J. S. Stein, "PVLIB Python 2015," in *2015 IEEE 42nd Photovoltaic Specialist Conference, PVSC 2015*, IEEE, 2015, pp. 1–5, ISBN: 9781479979448. DOI: 10.1109/PVSC.2015.7356005.

[45] G. W. Larson and R. A. Shakespeare, *Rendering with Radiance: The Art and Science of Lighting Visualization*. Morgan Kaufmann Publishers, 1998. [Online]. Available: https://floyd.lbl.gov/radiance/book/index.html.

[46] S. Crone, "Radiance users manual," vol. 2, no. November, 1992.

[47] G. J. Ward, "Measuring and modeling anisotropic reflection," *Computer Graphics (ACM)*, vol. 26, no. 2, pp. 265–272, 1992, ISSN: 00978930. DOI: 10.1145/142920.134078.

[48] J. T. Kajiya, "The Rendering Equation," vol. 20, no. 4, pp. 143–150, 1986.

[49] G. J. Ward, F. M. Rubinstein, and R. D. Clear, "A Ray Tracing Solution for Diffuse Interreflection," vol. 22, no. 4, pp. 85–92, 1988.

[50] G. J. Ward and P. S. Heckbert, "Irradiance gradients," *ACM SIGGRAPH 2007 Papers - International Conference on Computer Graphics and Interactive Techniques*, 2007. DOI: 10.1145/1401132.1401225.

[51] G. J. Ward, *Adaptive Shadow Testing for Ray Tracing*. [Online]. Available: https://floyd.lbl.gov/radiance/papers/erw91/erw91.html.

[52] M. R. Lewis, A. C. Russell, C. E. Valdivia, J. E. Haysom, M. I. Bertoni, and K. Hinzer, "Impact of Air Mass on Energy Yield Calculation for Bifacial Silicon Heterojunction Photovoltaic Modules in High-Latitude Conditions," *Conference Record of the IEEE Photovoltaic Specialists Conference*, vol. 2020-June, pp. 0371–0375, 2020, ISSN: 01608371. DOI: 10.1109/PVSC45281.2020.9300441.

[53] C. T. Li, "Development of field scenario ray tracing software for the analysis of bifacial photovoltaic solar panel performance," no. August, p. 145, 2016. [Online]. Available: http://www.ruor.uottawa.ca/handle/10393/35523.

[54] R. Perez, R. Seals, and J. Michalsky, "All-weather model for sky luminance distribution-Preliminary configuration and validation," *Solar Energy*, vol. 50, no. 3, pp. 235–245, 1993, ISSN: 0038092X. DOI: 10.1016/0038-092X(93)90017-I.